Effects of anharmonic driving on phase control of chaos and frequency-locking in nonlinear dynamical systems

by

VEZILE SAMUEL NGQUQU

submitted in accordance with the requirements
for the degree of

MASTER OF SCIENCE

in the subject

PHYSICS

at the

UNIVERSITY OF SOUTH AFRICA

SUPERVISOR: Professor A. E. Botha

September 2026

Declaration

Name: Vezile Samuel Ngququ

Student Number: 58386750

Degree: Master of Science (Physics)

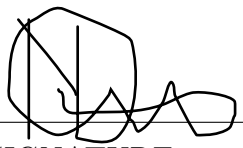
I declare that the dissertation "Effects of anharmonic driving on phase control of chaos and frequency-locking in nonlinear dynamical systems" is my own work and that all the sources that I have used or quoted have been indicated and acknowledged by means of complete references, and that any use of Artificial Intelligence (AI) has been fully disclosed.

I further declare that I submitted the dissertation to the appropriate originality detection system which is endorsed by Unisa and that it falls within the accepted requirements for originality.

I further declare that I have not previously submitted this work, or part of it, for examination at Unisa for another qualification or at any other higher education institution.

I further declare that where Artificial Intelligence (AI) tools have been used in the preparation of this thesis/dissertation, their use has been limited to ethical permissible support, has been fully disclosed, and does not replace my own original research, my independent critical thinking and analysis, or authorship responsibilities.

I understand that failure to disclose AI use, plagiarism and/or lack of academic integrity may constitute academic misconduct under Unisa's policies.



SIGNATURE

28/09/2026

DATE

Dedication

To my Mother and Father.

Acknowledgements

Thanks to my supervisor, Professor A. E. Botha, for his great mentorship, encouragement, and faith in my abilities throughout this journey. He provided me the flexibility to investigate the scientific subjects that have inspired me the most: anharmonic excitations and nonlinear phenomena in physics. I would also like to thank Jacques Auret from UNISA's ICT department for his assistance with High-Performance Computing (HPC), as well as the Department of Physics and the UNISA MD Bursary for financial support.

I would also like to thank my mentor, Sir Jan Ras, for his support, direction, and opportunities that have helped me grow personally and professionally. I am grateful to my grandmothers, Mantshitseng Tshabalala and Nampati Ngqugu, for their unfailing love, prayers, and encouragement. My sincere thanks to my uncles, Tloriso Mokhutle, Zwelinzima Ngqugu, Ditaba Mokhutle, and my sister, brother, S. Keketsi, T. Tsatsi, for their advice and encouragement. Finally, Pastor Moses Mabena, thank you for keeping me grounded in faith/purpose through your spiritual guidance/prayer during my academic journey. ("Camagu")

Abstract

The control of chaos in nonlinear dynamical systems is a frequently occurring practical problem. This thesis investigates how the type of excitation (harmonic versus anharmonic) affects chaos control and frequency locking in nonlinear systems. By anharmonic excitation, we mean a periodic excitation that includes the fundamental (harmonic) plus higher harmonics with non-trivial amplitudes. A novel periodic pulse function is developed as a convenient way of generating anharmonic (driving) excitations. Its duty cycle, smoothness, and symmetry can be controlled by three separate parameters. Using the Duffing oscillator as a prototype, extensive numerical simulations show that the harmonic drive can control chaos only in the sense of shifting it from one region in parameter space to another. Harmonic driving does not reduce the overall extent of the chaotic regions in the system's parameter space. In contrast, anharmonic driving can lead to an overall reduction in the extent of chaos in the system's parameter space. To see the effects of anharmonicity on locking more clearly, the sine circle map is considered. When the map function is replaced by the periodic pulse function, we find that there is generally a broadening in the Arnold tongue structures, again corresponding to an overall reduction of chaotic regions within the system's parameter space. These results are consistent with the intuitive idea that, when a nonlinear system is periodically driven, the locking is initiated through resonances that occur between the harmonics of the nonlinear system's oscillations and those of the drive. The present results are the first to show quantitatively that the richer harmonic spectrum of the anharmonic drive does increase the area over which locking occurs in the parameter space. Furthermore, the developed periodic pulse function provides a new way to generate the anharmonic signals that are needed for further studies about the onset of locking or the suppression of chaos in anharmonically driven nonlinear dynamical systems.

Key terms: Periodic pulse function, Phase control of chaos, Duffing oscillator, Frequency locking, Sine circle map, Harmonic excitation, Anharmonic excitation, Arnold tongues.

Contents

1 Introduction **2**

1.1 Literature Review . . . 3

1.1.1 Phase Control of Chaos . . . 3

1.1.2 Frequency Locking . . . 7

1.2 Problem Statement . . . 11

1.3 Limitations . . . 12

1.4 Outline . . . 12

2 Models and Methods **13**

2.1 Introduction . . . 13

2.2 Duffing Oscillator . . . 14

2.3 Sine Circle Map . . . 16

2.4 Lyapunov Exponents . . . 19

2.5 Periodic Pulse Function . . . 22

3 Phase Control of Chaos in the Duffing System **29**

3.1 Introduction . . . 29

3.2 Results . . . 30

3.3 Results of Gamma (γ) versus Beta (β) plane . . . 35

3.3.1 Comparison Summary for the Results of Gamma (γ) versus Beta (β) plane . . . 42

3.4 Results of Delta (δ) versus Gamma (γ) plane . . . 44

3.4.1 Comparison Summary for the Results of Delta (δ) versus Gamma (γ) plane . . . 51

4 Frequency Locking in the Sine Circle Map **53**

4.1 Introduction . . . 53

4.2 Results of the Standard Sine Circle Map . . . 54

4.3 Results of the Periodic Pulse Function Circle Map . . . 56

4.4 Comparison Summary for the Results Standard Sine and Periodic Pulse Function Circle Map 61

5 Conclusion **63**

Appendix **66**

A.1 Transformation of Simple Pendulum Equation 66

A.2 Python Code for Periodic Pulse Function 68

Bibliography **70**

Chapter 1

Introduction

Nonlinear dynamical systems can exhibit diverse behaviours ranging from periodic to chaotic. Furthermore, for a physical system that is chaotic, we may not, in general, be able to change all the parameters, since they are usually determined by the constituent materials. In many cases, however, it may be possible to control the chaos in a system by varying one of the parameters. Rather than changing the parameter, in certain situations it may be possible to control the chaos by perturbing the parameter, usually harmonically. This idea was proposed in the 1990s and is today known as the method of phase control of chaos.

A phenomenon that is closely related to the phase control of chaos is that of frequency locking. In this case, the nonlinear dynamical system's oscillations adjust themselves to become synchronised (locked) with those of the drive. The frequencies typically synchronise (lock) in some rational ratio p/q. This locking phenomenon occurs widely in many externally driven physical systems. In the case of the Josephson junction, for example, it gives rise to the harmonic ($q \leq p$) and subharmonic ($p < q$) Shapiro steps [1]. Frequency locking was originally studied using the sine circle map, and in the mathematical literature, the frequency-locked regions in the parameter space are usually called Arnold tongues [2] (instead of the term Shapiro steps, which is used in the case of the Josephson junction).

Outside of the Arnold tongues, the system generally exhibits quasiperiodic or chaotic behaviour. Consequently, near the edges of the Arnold tongues, the locking generally becomes more sensitive to noise. Deeper inside the Arnold tongues, the locking regions are generally more robust. The type of excitation used to achieve locking may also affect

the stability and extent of the locked regions. If we use only harmonic excitation (for example, a sinusoidal signal), it may produce the usual Arnold tongues. On the other hand, by driving the system with a signal that includes non-trivial higher harmonics, the Arnold tongues may change in shape. As we shall see in the next section, exactly how the shape of the Arnold tongues is affected by the nature of the drive is not something that has thus far been discussed much in the literature.

1.1 Literature Review

The literature reviewed in the following two subsections has been organised according to the aforementioned phenomena of interest.

1.1.1 Phase Control of Chaos

The phase control of chaos is a strategy to eliminate chaotic dynamics in certain nonlinear dynamical systems. The concept was introduced more than three decades ago by Ott, Grebogi, and Yorke (OGY) at the University of Maryland [3]. They showed that small, carefully designed perturbations could stabilise unstable motions inside chaotic attractors, and their pioneering work revealed that chaos is not totally random, but has some kind of deterministic structure underneath it, which could be used for control. The success of the OGY method led to much research on other control methods that might be easier to apply in real-world experiments. Among these developments, phase control became an attractive approach because it takes advantage of the sensitivity of nonlinear systems to appropriately timed external excitations.

Building on the OGY approach, subsequent research focused on developing experimentally viable control strategies that reduce the need for precise perturbation timing within the system. Pyragas, K. et al. [4] presented continuous time-delayed feedback control, which introduced a self-controlling feedback loop capable of stabilising unstable periodic orbits given information about the system's prior states. Unlike the OGY method, the Pyragas approach does not require explicit knowledge of the target orbit and is thus more appropriate for experimental implementation. Together, the OGY and Pyragas methods laid both theoretical and practical foundations for modern chaos control efforts to understand the mechanisms behind chaotic behaviour suppression.

As chaos control matured, researchers increasingly sought to integrate its theoretical and experimental efforts. Early research by Auerbach et al. [5], Morita et al. [6] and Grebogi et al. [7] demonstrated the existence of unstable periodic orbits within chaotic attractors. These researchers may have addressed the problem from different perspectives, but they all concluded that such orbits provide an underlying deterministic structure in what appears to be irregular motion. This became an essential component of current chaos-control theory because stabilising any unstable periodic orbit converts a chaotic trajectory into regular periodic behaviour.

On this basis, Boccaletti et al. [8] synthesised the rapidly expanding literature and argued that most chaos-control strategies are effective because they are closely related to the geometric structure of chaotic attractors. Although the various control approaches reviewed were different in implementation, all seem to be based on a common principle: exploitation of the intrinsic organisation of chaotic dynamics. This increasing understanding of the relationship between structure and controllability of attractors later on inspired phase-based control techniques, where one tries to regulate the chaotic behaviour by weak perturbations rather than large external control inputs.

Among the several methods of controlling chaos, phase control has drawn much attention because it has the potential to suppress chaotic behaviour with very weak perturbations. Early theoretical investigations by Qu et al. [9], Chacón et al. [10], and Yang et al. [11] showed that successful suppression of chaos is critically dependent on the phase relationship between external excitations and the response of the system. These studies agreed that phase is a basic control parameter and can even be more important than perturbation amplitude in some cases. This was the first major turning point, changing the focus from the amplitude of the control signal to the timing and synchronisation properties of the perturbation.

Following this idea, Chacón [12], Cao et al. [13], and Leung and Liu [14] considered the resonance mechanisms involved in phase control. Their results have repeatedly confirmed that small resonant perturbations could dramatically change the dynamical behaviour of a system, either suppressing or inducing chaos, depending on the phase angle. Although the importance of resonance effects was widely acknowledged, these experiments also showed that the characterisation of phase control success could not be restricted to perturbation amplitude, highlighting the intricate relationship between phase, resonance, and nonlinear system dynamics.

The theoretical predictions were experimentally validated at some point in time. Meucci et al. [15] showed that weak parametric perturbations can control chaos in

laboratory systems; Zambrano et al. [16] confirmed this with complementary numerical and experimental studies. Different systems and approaches were used, yet both arrived at the same conclusion: an appropriately chosen phase relationship could achieve a high degree of control with very low energy input. Their match gave strong proof that phase control is not just a theoretical idea but also a real way to change nonlinear dynamics.

After these validations, the studies moved beyond the simple suppression of chaotic oscillations. Seoane et al. [17] used phase control to avoid escapes in open dynamical systems, and Zambrano et al. [18] carried the technique to excitable systems. Although these applications are very different from standard chaos control problems, both showed that phase control has the capacity to influence transitions between different dynamical states and enhance stability in the system. This wider use implies that one should see phase control not only as an anti-chaos tool but also as a broad way to manage nonlinear behaviour in many kinds of dynamic systems.

As the field advanced, researchers increasingly sought to understand the dynamical structures that dictate how well phase control works. Chacón et al. [19] studied amplitude-modulated control strategies; Gonzalez-Henao et al. [20] took phase control ideas into quantum systems. The works of Freire et al. [21], Pugliese et al. [22] and Junges et al. [23] stressed stability structures, periodic organisation in parameter space diagrams, and how these things help determine how a system will respond. These studies suggest that successful phase control is closely related to the stability landscape of a nonlinear system. However, there are differences regarding which mechanisms are most important: some emphasise resonance structures, others phase synchronisation, and still others the geometry of stability boundaries.

In the last few years, the focus of the research on phase control has shifted towards optimisation of phase control strategies. Meucci et al. [24] demonstrated that certain ideal phase settings can improve control efficiency in damped-driven Duffing oscillators. Martinez et al. [25, 26] demonstrated that the shape of the excitation is crucial to improving the control performance using minimal parameter combinations with incommensurate forcing. Although both studies agreed that there is more to phase control than simply the amplitude of the perturbation, they disagreed on which mechanism is most important. Meucci et al. [24] worked on optimal phase matching, while Martinez et al. [25, 26] focused on excitation structure and frequency interactions. Therefore, it is still an open topic in the research on phase control whether phase relationships, resonance processes, or driving properties are most relevant.

Against this background, the Duffing oscillator provides a useful framework for

investigating the role of phase relationships, excitation characteristics, and resonance mechanisms in the control of chaotic dynamics. The Duffing oscillator is used to test novel approaches and as an approximation for physical systems [27–30]. Martinez et al. [26] studied, numerically, the impulse-induced chaos control scenario with additive noise in the Duffing equation, given by,

$$\ddot{x} = x - \beta[1 + \eta f(t)]x^3 - \delta\dot{x} + \gamma\cos(\omega t) + \sqrt{\sigma}\xi(t). \tag{1.1}$$

Here, all the parameters $(\beta, \eta, \delta, \gamma, \sigma)$ are positive real numbers and the equation has been written in dimensionless form. The term $\xi(t)$ represents added Gaussian white noise and $f(t)$ is a unit-amplitude T_p-periodic suppressory excitation (SE) that can be described in terms of Jacobian elliptic functions [26]. Martinez et al. [26] analysed the impulse-induced chaos control situation without the added noise, by writing the equation as a first-order autonomous system,

$$\begin{aligned} \dot{u} &= v, \\ \dot{v} &= u - \beta[1 + \eta f(\frac{w}{\omega})]u^3 - \delta v + \gamma\cos w, \\ \dot{w} &= \omega. \end{aligned} \tag{1.2}$$

The Duffing oscillator is one of the most popular models in nonlinear dynamics because it can describe basic phenomena such as nonlinear resonance, bifurcations, jump phenomena, and chaos. Peleg et al. [31] and Brennan et al. [32] showed that, unlike linear oscillators, the Duffing system may have more than one steady-state solution and may also suddenly change its vibration amplitude; this response depends strongly on excitation frequency and nonlinearity. Although these studies considered different aspects of nonlinear resonance, they together established the Duffing oscillator as a good model for complex dynamical behaviour under external forcing.

The fact that the Duffing oscillator can serve as a model for many different physical systems lends weight to its widespread use. Johannessen et al. [33] proved that a drive-damped nonlinear pendulum could be expressed in terms of a Duffing equation. At the same time, Shukrinov et al. [34] came up with an approximate Duffing equation related to superconducting-ferromagnetic Josephson junctions. Numerous analytical and numerical techniques have been developed to explore Duffing dynamics, such as the exponential time differencing technique, the target function approach, and the Laplace decomposition method [28, 30, 35]. One conclusion emerged from all of these studies: Strongly nonlinear systems can be studied using the Duffing oscillator, a realistic yet theoretically straightforward model.

More than three decades of research on phase control reveal an important limitation that has been evident in the literature until now. The early theoretical investigations by Qu et al. [9], Chacón et al. [10, 12], and Yang et al. [11], followed by experimental studies conducted by Meucci et al. [15, 24] and Zambrano et al. [16, 18], led to recent optimisation strategies proposed by Martinez et al. [25, 26]. The overwhelming majority of these investigations have considered systems driven by harmonic excitations. Nevertheless, anharmonic excitations affect the great majority of nonlinear systems in physics and engineering, producing more complex dynamic reactions and additional nonlinear interactions. Although Martinez et al. [25, 26] initiated studies using forcing functions beyond harmonic excitations, there is an incomplete understanding of how anharmonic driving impacts the efficiency of phase control. This motivates the present study on phase control in anharmonically driven nonlinear systems and its effect on their frequency locking behaviour.

1.1.2 Frequency Locking

Since phase control mechanisms depend on the interaction between an external excitation and the intrinsic oscillatory dynamics of a nonlinear system, understanding frequency locking is the key. Frequency locking gives the theoretical basis for how phase control can suppress chaos in favour of stable periodic motion. The phenomenon is frequently demonstrated using Arnold tongues, named after Vladimir Arnold in 1961, who introduced it while exploring mappings of the circle onto itself and periodic driving influence on nonlinear oscillators [2]. Arnold showed that when an oscillator is subjected to external periodic forcing, regions emerge in parameter space where the oscillator synchronises with the forcing frequency via rational frequency ratios. When plotting these synchronisation regions, one obtains tongue-shaped structures extending from rational frequency ratios known as Arnold tongues. Further studies by Jensen and Krishna [36] confirmed that such structures arise in a wide variety of nonlinear systems, providing universal descriptions for synchronisation and frequency locking phenomena.

Frequency locking occurs when the natural frequency of an oscillator is adjusted to an externally applied periodic forcing such that a stable ratio between the two frequencies is achieved [37, 38]. This phenomenon represents one of the most fundamental forms of synchronisation and appears in everything from physics and engineering to chemistry and biology. Then Pikovsky et al. [38] determined that synchronisation arises when the interaction between oscillatory components becomes strong enough to overcome their mismatch in natural frequency, while Strogatz et al. [37] considered frequency locking

as a universal mechanism for collective dynamical behaviour. Therefore, Arnold tongue diagrams provide a natural parameter space representation of regions where frequency locking occurs, as this depends on coupling strength and forcing frequency.

Arnold introduced the sine circle map in his early work on periodically forced oscillators and frequency locking [2]. The model describes the dynamics of a phase variable under the influence of both an intrinsic frequency and a nonlinear coupling term; thus, it serves as a simple mathematical representation for competing oscillatory processes. Arnold showed that the parameter space of the system supports several regions of synchronisation (now known as Arnold tongues), where ratios between frequencies involved are rational numbers. These results made the circle map establish itself as a basic model for studies concerning phase locking, synchronisation, and transitions between regular and complex dynamical behaviour.

Further studies generalised Arnold's work and established that frequency locking is a special case of more general nonlinear phenomena. Feigenbaum et al. [39] and Jensen et al. [40] showed that resonance interactions lead, in a universal manner, to transitions from quasiperiodicity to chaos. Though they used different approaches, both studies agreed that the circle map is an appropriate model for understanding how order and chaos coexist in the vicinity of synchronisation boundaries. These results were later confirmed by Kuznetsov et al. [41] when they worked on quasiperiodic critical phenomena and further established the universal character of resonance interactions in circle map dynamics.

The sine circle map was further endorsed by Feudel et al. [42], who used it for analysing phase-locking in quasiperiodically forced systems. Their results proved that Arnold tongues and bifurcation structures are efficient tools for characterising synchronisation behaviour. Pikovsky et al. [43] reached the same conclusion from a different perspective; they considered synchronisation as a universal property of nonlinear systems. Glass et al. [44] indicated its importance in biological and physiological processes. All these studies come to support frequency locking not as something specific to certain physical systems but rather as an organising principle of nonlinear dynamics that has general applicability.

Donato et al. [45] provided practical evidence of the circle map when they demonstrated how one can use the topological structure of Arnold tongues to create effective strategies for phase-locking control. In this way, the circle map was transformed from a theoretical model into a helpful tool to understand and regulate synchronisation phenomena. Hence, this study uses the sine circle map as its representative for the discrete

dynamical system protocol to explore frequency locking. The discussion in the following provides its mathematical formulation and indicates the subsequent manifestations of the dynamics of Arnold tongues and rotation numbers. The following discussion presents the mathematical formulation first and then discusses how Arnold tongues and rotation numbers come into play in dynamics naturally.

The long-term dynamics of the circle map are characterised by a winding number that measures the average advancement of the phase per iteration. The oscillator locks its frequency to that of another if the winding number is rational ($\Omega = p/q$), in which case it follows a periodic orbit. An irrational winding number corresponds to quasiperiodic motion with trajectories that never exactly repeat. Then, as the coupling strength increases, neighbouring resonance regions grow until they eventually overlap, making dynamics more complicated and possibly leading to chaos via resonance interaction [39–44]. The set of these resonance regions gives rise to what is known as an Arnold tongue structure, and this serves as a roadmap for understanding synchronisation behaviour in nonlinear dynamical systems.

Frequency locking has practical importance that goes well beyond theoretical models; it has been seen in actual experiments with many physical systems. Wiesenfeld et al. [46] illustrated the application of the Kuramoto model to the lumped-circuit equations for a series array of zero-capacitance Josephson junctions, achieving perfect frequency locking. They analytically determined the percentage of junctions that frequency-lock as a function of various circuit parameters. Despite differing natural frequencies, connected nonlinear oscillators can synchronise spontaneously. The Josephson array exhibits two transitions: the emergence of dynamical order and complete frequency locking in the second transition. Both transitions are considered experimentally achievable with current technology.

In Fig. 1.1, we can see that a Josephson junction exhibits regions of constant average voltage in its $I - V$ characteristic due to frequency locking with an external source (typically microwave irradiation). In this case, the Arnold tongues are called Shapiro steps [47]. Firstly, the Amplitude of the drive controls the widths of the Shapiro steps, following a Bessel function dependence. Second, the direct current bias (I) controls the junction frequency.

The common occurrence of Arnold tongues and frequency locking in systems as diverse as circle maps, coupled oscillators, and Josephson junctions speaks to the fact that synchronisation is a phenomenon of universal character in nonlinear dynamics. Most theoretical and experimental work has been done on systems driven by purely

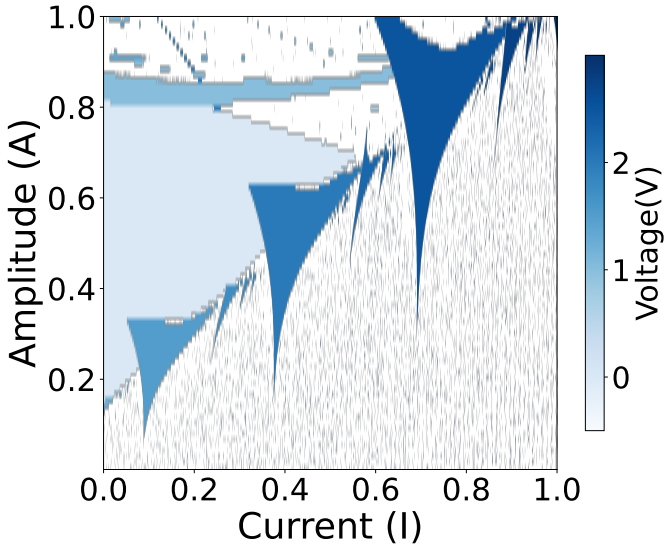


Figure 1.1: Shows Shapiro steps in Josephson Junctions with IV properties. As a result, increasing the current causes the junctions to move faster and quicker, and therefore the frequency increases. Meanwhile, decreasing the current causes the junction to run at a slower pace and decreases the frequency.

harmonic excitations. Under these conditions, the resulting structures of the Arnold tongues and locking regions are quite well understood. Much less attention has been paid to systems under anharmonic excitations, although it is well known that anharmonic excitations are very often found in a large number of physics and engineering applications. Since anharmonic driving introduces extra frequency components with their nonlinear interactions, it can change the mechanisms of resonance, structures of resonances, and geometry for Arnold tongues significantly. It is thus an important open problem to know how frequency locking develops under anharmonic excitations; this gives rise to the present study investigating the effect of such excitations on the behaviour of frequency locking, together with associated structures for Arnold tongues in nonlinear dynamical systems.

1.2 Problem Statement

Nonlinear dynamical systems are fundamentally characterised by synchronisation and locking. As such, their natural oscillation frequencies also depend on their oscillation amplitudes, enabling them to adapt and lock onto a drive signal, i.e., to become synchronised with the drive. In this research, we highlight that, in the literature, most nonlinear systems have usually been driven only by simple harmonic signals; the rationale being that any more complicated drive signal can always be constructed as a Fourier series of anharmonic signals. However, few works have incorporated anharmonicity into the drive, leaving the unexplored question of how these complex harmonics may affect locking. In this work, we aim to investigate the effect of using a drive signal with a more complex harmonic structure. We focus on how such a drive signal may affect locking and chaos control in nonlinear systems. To study its effects, we use two classical systems as prototypes: (i) phase control of the Duffing oscillator and (ii) locking in the sine circle (iterative) map.

This work introduces a new periodic pulse function (PPF) that we invented to test the effect of anharmonicity on the phase control of chaos and frequency locking. The problem is not only how the system responds to anharmonic signals or the impact of anharmonic driving on phase control of chaos and frequency locking in nonlinear dynamical systems, but also the usefulness and effectiveness of the periodic pulse function in testing various systems. We will investigate the effects of duty cycle, smoothness, and symmetry factor on suppression in a non-elliptical way by using a shape-changing periodic pulse function that we constructed, instead of utilising elliptic functions. Then, we will use this complex signal (PPF) for frequency locking because it has a complex harmonic spectrum with higher Fourier harmonics. As a result, we anticipate that the signal will have a higher probability of locking onto the chaotic system's frequency and expanding the Arnold Tongues. Due to its non-linearity and frequency modulation, many conventional signal processing techniques forbid anharmonic behaviour.

The purpose of this work is to advance our understanding of anharmonic forcing actions on system behaviour by exploiting the intriguing qualities of the periodic pulse function. These qualities offer clear advantages in dealing with nonlinearity and transient behaviours in dynamical systems. This work explores the use of the periodic pulse function in developing analytical frameworks and computational models to analyse complex anharmonicity in various scientific and technical disciplines, using numerical tests and theoretical demonstrations.

1.3 Limitations

This study may examine several systems, but we have limited it to just two due to effective dynamical system protocols: the Duffing system is a good protocol for continuous dynamical systems, and the sine circle map is a good protocol for locking discrete dynamical systems.

1.4 Outline

The subsequent chapters are laid out as follows. In Chapter 2, we present the Duffing system model, a popular model in nonlinear dynamics for controlling chaos. We show the sine circle map model, a one-dimensional nonlinear iterative map which, since then, has been used as a standard model for synchronisation, quasiperiodicity, and transition into chaos. We demonstrate the fundamental mechanism for the Lyapunov exponent as a measure and detect chaos or stability in a nonlinear dynamical system. We also introduce an anharmonic drive, namely the periodic pulse function (PPF), and its mathematical properties.

In Chapter 3, we present a comparison of phase control of chaos using the Duffing system as a prototype, where the effectiveness of the periodic pulse function is evaluated against the elliptic function-based control signal.

Chapter 4 compares the frequency locking (Arnold Tongues) using the sine circle map, where the standard harmonic map is compared with the periodic pulse function circle map through analysis of Arnold tongue structure.

Lastly, Chapter 5 summarises the major findings of this study, their implications for chaos control and frequency locking, limitations of the current research, and suggestions for future research.

Chapter 2

Models and Methods

2.1 Introduction

The previous chapter introduced phase control of chaos and frequency locking in nonlinear dynamical systems by discussing their theoretical underpinnings and the limitations of current studies. The literature review revealed that most studies on phase control of chaos and frequency locking have focused on harmonically driven systems, while the influence of anharmonic excitations remains underexplored. To analyse this problem rigorously, it is imperative to establish the mathematical and physical framework underlying the analysis presented in this thesis.

This chapter introduces the main models and analytical methods used in the entire study. First, the Duffing oscillator is introduced as a prototypical nonlinear system for studying phase control of chaos because of its rich dynamic behaviour, which includes periodic, quasi-periodic, and chaotic responses. Secondly, basic mechanisms of frequency locking are described via sine circle maps that fundamentally describe synchronisation phenomena and how Arnold tongues are formed. Since understanding frequency locking is very crucial to knowing how external excitations interact with intrinsic oscillations of the system, it is theoretically linked very importantly to phase control mechanisms. The other important aspect introduced here is the Lyapunov exponent, a quantitative measure for differentiating between chaotic and regular motions, so that dynamic transitions under different forcing conditions can be identified.

Lastly, this chapter describes the periodic pulse function (PPF), which is considered an anharmonic driving function in this work. We emphasise its mathematical proper-

ties and Fourier-series representation because its governing parameters systematically control the complexity of excitation. This makes PPF a convenient setting for studying how deviations from standard harmonic forcing affect phase control of chaos, frequency locking, and related dynamical behaviours of nonlinear systems.

2.2 Duffing Oscillator

The Duffing oscillator has been one of the most widely studied nonlinear dynamical systems, and has consequently become a basic model for the study of such complex phenomena as bifurcations, chaos, synchronisation, and nonlinear resonance [48, 49]. The Duffing equation is a significant model for driven nonlinear oscillators as it may demonstrate three unique forms of dynamical behaviour: periodic, quasiperiodic, and chaotic, when subjected to external forces. It applies to mechanical vibrations, electrical circuits, structural engineering problems, as well as issues in nonlinear control theory. For this study, we take advantage of the rich dynamical behaviour possible with a Duffing oscillator to examine phase control of chaos, since this permits very systematic variation of both external perturbation and forcing function influences. The physical realisation that corresponds to the mathematical form known as the Duffing equation is easily understood from that description: it corresponds to one of the simplest examples of a driven damped nonlinear pendulum, namely motion through an angle by means of gravity acting on its mass, presented in detail by Davis [48].

Consider the equation for a simple pendulum,

$$\frac{d^2\theta}{dt^2} + \frac{g}{l}\sin\theta = 0 \tag{2.1}$$

where θ is the angle made with respect to the vertical direction, m is the mass of the pendulum, l is its length, and g is the Earth's gravitational acceleration. By substitution $g/l = k^2$, Eq. (2.1) becomes

$$\frac{d^2\theta}{dt^2} + k^2\sin\theta = 0 \tag{2.2}$$

By introducing the transformation, $y = \sin(\theta/2)$, Eq. (2.2) becomes [48]

$$\frac{d^2y}{dx^2} = \ddot{y} = ay + by^3. \tag{2.3}$$

where $a = -k^2(1 + \sin^2\theta_m/2$, $b = 2k^2$ and θ_m is the amplitude (see, Appendix A.1 for further details). Equation (2.3) can be integrated by elliptic functions [48]. A

generalisation of Eq. (2.3) is given by,

$$\frac{d^2y}{dx^2} + k\frac{dy}{dx} + ay + by^3 = f\cos(\omega x) \tag{2.4}$$

where $k\dot{x}$, ($k \geq 0$) is a viscous damping force and f is the amplitude of a harmonic drive with frequency ω. [35]. The term ay represents a linear restoring force, while by^3 is a non-linear (conservative) force. Eq (2.4) is commonly referred to as the Duffing equation, since it was the subject of the first systematic study of its kind conducted in 1918 by G. Duffing as part of an extensive investigation of forced vibrations [31, 48].

The Duffing equation represents the motion of a classical particle in a double-well potential given by

$$V(x) = -\frac{a}{2}x^2 + \frac{b}{4}x^4 \tag{2.5}$$

as shown in Fig. 2.1. The potential in Eq. (2.5) is relevant because it can model bi-stability and spontaneous symmetry breaking mathematically.

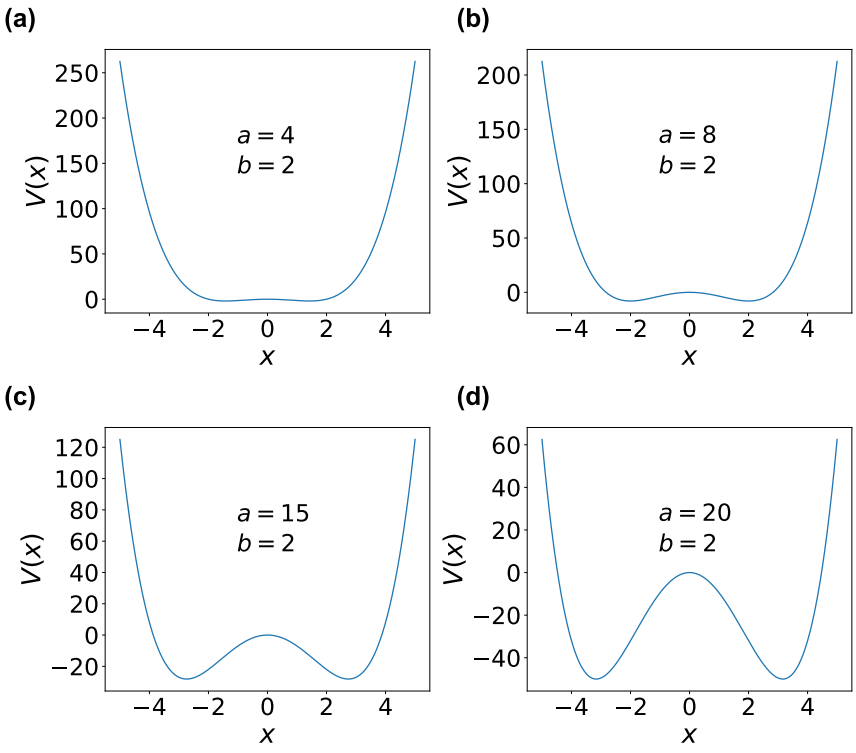


Figure 2.1: The double well potential given by Eq. (2.5) and four different choices of the parameters. In (a) and (b) the potential is approximately parabolic, while in (c) and (d) the central peak is more pronounced. Physically, it is the sporadic crossing over between the two wells formed on either side of the central peak that gives rise to the chaotic behaviour associated with the Duffing system.

Apart from its role in nonlinear dynamics, the Duffing oscillator has become a canonical model for chaos-control scenarios. Meucci et al. [24] proved that carefully chosen phase perturbations can control chaotic motion, while Martinez et al. [25, 26] improved control performance with optimal parameter selection and incommensurate excitations. Although these studies emphasised different mechanisms of control, they consistently identified the Duffing oscillator as a good model for analysing phase control strategies. Most investigations were limited to harmonically driven systems; thus, the effect of anharmonic excitations remains relatively unexamined until now. This motivates our study, which uses the Duffing oscillator as a representative continuous nonlinear system to look at the influence of anharmonic driving on phase control behaviour. The next section addresses this continuous-system perspective by presenting the sine circle map as a canonical discrete dynamical-system model, which has been used extensively in theoretical studies related to frequency locking and Arnold tongue formation.

2.3 Sine Circle Map

The Duffing oscillator has been used as a standard prototype in various studies concerning phase control within continuous nonlinear systems. However, studies on frequency locking necessitate a model that can describe how phase relationships evolve between oscillators interacting with one another. In this context, the sine circle map has become one of the most widely known and used examples of discrete dynamical system models. This not only makes it significant but also interesting because it captures what happens at the most basic level in synchronisation, resonance interaction, and development into areas of frequency locking. That is why this study naturally pairs up with a Duffing oscillator.

Following the discussion in Hilborn et al. [50], consider the general iterated map given by

$$\theta_{n+1} = f(\theta_n) \tag{2.6}$$

where the function $f(\theta_n)$ is periodic in the angle θ_n. When the map function is linear, Eq. (2.6) becomes

$$\theta_{n+1} = f(\theta_n) = \theta_n + \Omega \tag{2.7}$$

Mathematically, to study the emergence of frequency locking, Arnold introduced the sine circle map, a one-dimensional nonlinear iterative map which, since then, has been used as standard modelling for synchronisation, quasi-periodicity, and transition into

chaos [2]. The map is given by

$$\theta_{n+1} = \theta_n + \Omega - \frac{K}{2\pi}\sin(2\pi\theta_n) \tag{2.8}$$

where Ω denotes the driving frequency, K coupling strength, and θ_n is the phase variable [42, 45, 50]. At $K = 0$, the sine circle map reduces to the simple linear map of Eq. 2.7. Then, with $K > 0$, the parameter K is a measure of the strength of nonlinearity. Therefore, varying K and Ω, the circle map captures those essential mechanisms responsible for the frequency locking and formation of Arnold tongues.

However, only systems with their own independent fundamental frequencies are described by this map. Donato P. et al. [45] and Feudel U. et al. [42] agreed with the same map in Eq. (2.8), because it is necessary since their objective is to examine the nonlinear relationship with the map of Eq. 2.7. The bifurcation structure for the circle map was originally reviewed by Feudel U. et al. [42], taking into account only Eq. (2.8) with phase-lock without forcing. Its behaviour, dependent on the parameters Ω and K, is well-known [40, 42, 51]. The sine circle map becomes non-invertible above the critical line $K = 1$, and chaos can occur. For $K < 1$, the mapping is invertible, exhibiting two distinct behaviours: two-frequency quasiperiodic motion, characterised by an invariant circle as the attractor, and phase-locked periodic motion, where the attractor comprises a set of points on this invariant circle. It can be demonstrated that chaos is also excluded for the quasi-periodically forced system with the coupled pair of equations (Eq. (2.7), Eq. (2.8)) defining the dynamical system when $K \leq 1$. Chaotic motion is not taken into account in this work, as the authors limited themselves to nonlinearities below the critical line $K = 1$. The rotation number W, which is described by both periodic and quasiperiodic behaviour:

$$W = \lim_{n\to\infty}(\frac{\theta_n - \theta_0}{n}) \equiv \Omega \tag{2.9}$$

A frequent occurrence in non-linear interactions between two or more "oscillators" is frequency locking [50]. The frequency f_1 for oscillator number 1 and f_2 for oscillator number 2 characterise each oscillator (The oscillators could be different "modes of motion" inside the same physical system, or they could be physically independent oscillators for two different pendulum clocks, for instance). Hilborn R.C. et al. [50] refer to two oscillators as frequency-locked (mode-locked or phase-locked) if they are proportional over a range of control parameter values, i.e., $\frac{f_2}{f_1} = \frac{p}{q}$ (p, q integers) over this parameter range. To comprehend the physical meaning of frequency-locking, two aspects of non-linear systems must be remembered:

First, the actual oscillation frequency of a non-linear oscillator is often determined by the oscillator's motion amplitude. Therefore, if a system parameter changes, one would normally expect the frequency of a non-linear oscillator to change as well because the oscillation's amplitude will also vary due to the parameter change. Given this, one may anticipate that obtaining a specific frequency ratio, such as p/q, would require extremely precise parameter values to be established. On the other hand, over a range of parameter values, the same ratio p/q holds in frequency locking [50].

Second, a Fourier series of sinusoidal oscillations can be used to describe the time behaviour of an oscillator for a given set of parameter values. Therefore, they can write for oscillator number 1

$$x_1(t) = \sum_{k=1}^{\infty} B_k \sin\left(2\pi k f_1 t + \phi_k\right) \tag{2.10}$$

where the integer k is positive. The phase of the frequency kf_1 is ϕ_k, and the amplitude associated with it is B_k. The important thing to remember is that motion may be seen as consisting of periodic motion with amplitudes B_1,B_2,B_3,... and frequencies f_1,$2f_1$,$3f_1$,... In a similar vein, oscillator number 2 is explained by

$$x_2(t) = \sum_{j=1}^{\infty} C_j \sin\left(2\pi j f_2 t + \psi_j\right) \tag{2.11}$$

The pth harmonic of f_1, or pf_1, is equal to the qth of f_2 ($pf_1 = qf_2$), if the two frequencies, f_1 and f_2, are in accordance with the frequency $\frac{f_2}{f_1} = \frac{p}{q}$. This equivalence indicates that the qth harmonic of f_2 can "tickle" the motion related to the pth harmonic of f_1 to produce a form of resonance effect since the two oscillators are interacting. (Note that there will be an unlimited number of overlap frequencies with $nqf_2 = npf_1$ and $n = 1, 2, 3, ...$ if $f_2 = pf_1$. None of the harmonics would coincide, and mutual resonance would not occur if the frequencies were incommensurate) [50, 52].

These ideas allow us to state that frequency-locking happens anytime the oscillator's tendency to change frequencies (also caused by nonlinearity) is subordinated to the resonance interaction of harmonics. This picture leads us to believe that one of the frequencies is changed (say, f_1, which could be the oscillator driving the system). At the same time, the strength of the non-linearity is kept constant, and the frequencies should lock for a range of f_1 values before either unlocking (becoming incommensurate) or jumping to another integer ratio for the new value of f_1. It is also possible to hypothesise that the range of f_1, in which frequency lock-up occurs, may be wider if the ratio p/q has tiny p and small q, such as $1/2, 2/3$, but not $17/19$. This is assuming that they have eliminated all common divisors. The idea behind this is that in general

(though not always) the amplitudes of motion are linked to the low harmonics, which are the low values of k and j in Eq. (2.10) and Eq. (2.11) and are bigger than those for the higher frequency harmonics[50].

Although a wide range of literature exists on frequency locking and Arnold tongues, most studies of the sine circle map have focused on systems driven by fixed harmonic excitations. Notably, Arnold [2], Feigenbaum et al. [39], Jensen et al. [40], Feudel et al. [42], and Hilborn [50] investigated systems under such driving conditions. This has led to detailed investigations of synchronization regions, rotation numbers, quasi-periodicity, and transitions to chaos. However, most nonlinear systems encountered in practical applications are subjected to excitations that are not purely harmonic but may carry more complex temporal structures. As a result, the effects of anharmonic driving on frequency locking behaviour, Arnold-tongue organization, and synchronization mechanisms have received relatively little attention within the sine circle map framework. This motivates our study, which uses the sine circle map as a representative discrete nonlinear system to look at the influence of anharmonic driving on frequency locking behaviour.

2.4 Lyapunov Exponents

The main goal of this study is to analyse the effect of anharmonic excitation on phase control and frequency locking phenomena; a reliable measure of the resulting dynamical behaviour is needed. In both the Duffing oscillator and sine circle map, this measure will be implemented using Lyapunov exponents, which serve as a quantitative indicator for stability and chaos. Consider a nonlinear system of ordinary differential equations given by

$$\dot{x} = f(x), \tag{2.12}$$

where x represents the state vector and $f(x)$ denotes a nonlinear vector field. A nearby trajectory can be expressed as $x(t) + p(t)$ in order to evaluate the development of a small perturbation p about a fiducial trajectory $x(t)$. The corresponding equation is

$$\frac{d}{dt}[x(t) + p(t)] = f[x(t) + p(t)], \tag{2.13}$$

Using a first- order Taylor expansion of $f(x + p)$ about the fiducial trajectory $x(t)$

$$f(x + p) = f(x) + \frac{d}{dt}p + O(|p|^2), \tag{2.14}$$

Therefore,

$$\dot{x} + \dot{p} = f(x) + \frac{d}{dt}p + O(|p|^2), \tag{2.15}$$

Substituting Eq. (2.12) to Eq. (2.15), the evolution of the perturbation is given by

$$\dot{p} = \frac{d}{dt}p + O(|p|^2), \tag{2.16}$$

Assuming that the perturbation is small enough that the higher-order terms can be neglected. The corresponding linearised system becomes

$$\dot{p} = \partial_x f(x)p, \tag{2.17}$$

where $\partial_x f(x)$ is the Jacobian matrix of the non-linear function f, evaluated along the fiducial trajectory $x(t)$, and p is the perturbation vector shown in Fig. 2.2. The fiducial trajectory, defined by non-linear equations, represents the centre of the sphere [53]. As the system evolves, the initial spherical set of nearby trajectories is transformed into an ellipsoid. The lengths of the principal ellipsoidal axes are used to define the *ith* one-dimensional Lyapunov exponent [53–57].

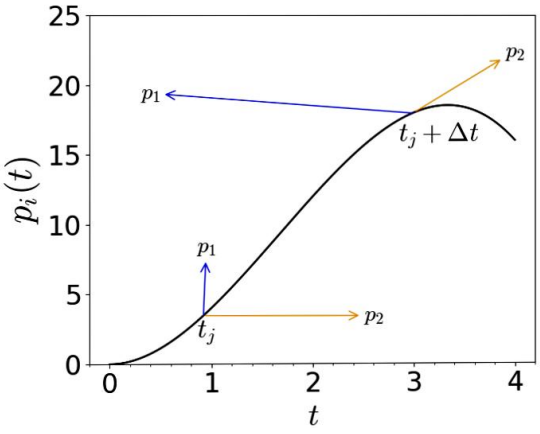


Figure 2.2: The fiducial trajectory is the solution of Eq. (2.12) and the perturbation vectors (p_1, p_2) evolve according to the linearised system Eq. (2.17); we measure the growth rate of each vector as the system evolves over each time step.

The definition of the *ith* Lyapunov exponent is

$$\lambda_i = \lim_{t\to\infty} \frac{1}{t} \ln \frac{|p_i(t)|}{|p_i(0)|} \tag{2.18}$$

where $p_i(t)$ is the perturbation's magnitude along the *ith* principal direction. The Lyapunov exponents are conventionally arranged in descending order

$$\lambda_1 \geq \lambda_2 \geq ... \geq \lambda_n \tag{2.19}$$

When λ_i is positive, nearby trajectories along the corresponding direction indicate exponential divergence, while when it is negative, they indicate exponential contraction. Neutral separation in that direction is indicated by a zero exponent. For a 2-dimensional phase-space system, the sum of the two Lyapunov exponents is related to the asymptotic evolution of an infinitesimal area formed by two independent perturbation vectors[57]:

$$\lambda_1 + \lambda_2 = \lim_{t\to\infty} \frac{1}{t} \ln \frac{|A_i(t)|}{|A_i(0)|} \tag{2.20}$$

Where $A_i(t)$ is the area of the parallelogram spanned by the two perturbation vectors. Consequently, the sum $\lambda_1 + \lambda_2$ describes the exponential rate of expansion or contraction of an infinitesimal area in phase space. Consider the Lyapunov exponent as the time-average exponential growth rate of a perturbation. If the perturbation grows exponentially at a constant rate λ_i, then

$$|p_i(t)| = |p_i(0)|e^{\lambda_i t} \tag{2.21}$$

and at a subsequent time $t + \Delta t$

$$|p_i(t + \Delta t)| = |p_i(0)|e^{\lambda_i t + \Delta t} = |p_i(0)|e^{\lambda_i t} e^{\lambda_i \Delta t} \tag{2.22}$$

Dividing Eq. (2.22) by Eq. (2.21) gives

$$\frac{|p_i(t + \Delta t)|}{|p_i(t)|} = \frac{|p_i(0)|e^{\lambda_i t} e^{\lambda_i \Delta t}}{|p_i(0)|e^{\lambda_i t}} = e^{\lambda_i \Delta t} \tag{2.23}$$

However, applying ln to both sides and solving for the finite-time Lyapunov exponent gives

$$\ln\left(\frac{|p_i(t + \Delta t)|}{|p_i(t)|}\right) = \ln\left(e^{\lambda_i \Delta t}\right) = \lambda_i \Delta t \tag{2.24}$$

Therefore,

$$\lambda_i = \frac{1}{\Delta t} \ln\left(\frac{|p_i(t + \Delta t)|}{|p_i(t)|}\right) \tag{2.25}$$

Let $t_j = j\Delta t$ for a numerical trajectory divided into M time intervals of equal duration Δt. The logarithmic growth factor over the M intervals added together gives

$$\lambda_i = \lim_{M\to\infty} \frac{1}{M\Delta t} \sum_{j=1}^{M} \ln\left(\frac{|p_i(t_j + \Delta t)|}{|p_i(t_j)|}\right) \tag{2.26}$$

Since the total observation time is

$$T = M\Delta t \tag{2.27}$$

Eq. (2.26) can equivalently be written as

$$\lambda_i = \lim_{T\to\infty} \frac{1}{T} \sum_{j=1}^{M} \ln\left(\frac{|p_i(t_j + \Delta t)|}{|p_i(t_j)|}\right) \tag{2.28}$$

Assuming that the divergence of nearby trajectories can be described within the linearised approximation, two trajectories in phase space with an initial separation vector $p(t_j)$ evolve according to the linearised dynamics. The Lyapunov exponent therefore measures the average exponential rate at which the separation between the trajectories increases or decreases with time [57].

2.5 Periodic Pulse Function

Now that the techniques for quantifying dynamical behaviour via Lyapunov exponents have been discussed, the focus can shift to the forcing mechanism itself. Rather than making use of Fourier series expansions, here we introduce a periodic pulse function with three parameters to facilitate our study of how anharmonicity in the drive affects the non-linear dynamics in comparison to the well-studied case of harmonic driving in the same model. To this end, we have developed the periodic pulse function (PPF) as a linear combination of sigmoid functions $(1/\left[1+\exp(-x)\right])$, with appropriate shifting and scaling. The function is given by

$$\begin{aligned} P(t) = \frac{\text{sign}(f(t))}{A}\Bigg[A_0 + \frac{1}{1+\exp\left(\alpha\left[|f(t)| - \beta - 1 + r(\beta-1)\right]\right)} \\ - \frac{1}{1+\exp\left(\alpha\left[|f(t)| + \beta - 1 + r(\beta-1)\right]\right)}\Bigg], \end{aligned} \tag{2.29}$$

where $\alpha = 1.75686487/\left(s+\varepsilon\right)$ is defined in terms of the smoothness parameter $s \in [0,1]$, $\beta = d + \varepsilon$ in terms of the duty cycle parameter $d \in [0,1]$ and the symmetry factor $r \in [0,1]$. In the definitions of α and β, a small parameter $\varepsilon = 10^{-12}$ has been introduced for numerical convenience, to avoid division by zero in the definition of α when $s = 0$.

The quantity A in Eq. (2.29) is the normalisation factor used in the numerical implementation. It is given by

$$A = \frac{1}{1+\exp(-\alpha\beta)} - \frac{1}{1+\exp(\alpha\beta)} + A_0. \tag{2.30}$$

The constant A_0 is introduced to offset the two sigmoid terms. In the numerical implementation used in this thesis, it is defined by

$$A_0 = -\frac{1}{1+\exp\left[\alpha(-\beta-1)\right]} + \frac{1}{1+\exp\left[\alpha(\beta-1)\right]}. \tag{2.31}$$

and the sawtooth function [58],

$$f(t) = \frac{4}{\pi}\tan^{-1}\left[\frac{\cos(t/2)}{\sin(t/2)}\right]. \tag{2.32}$$

The normalisation factor A provides the normalisation required for the resulting PPF to have unit amplitude. Like ordinary trigonometric functions, $\sin(t)$ and $\cos(t)$, $P(t)$ also has a period of 2π and a unit amplitude. For example, in Fig. 2.3, we have plotted it in four different combinations of parameters. Looking at Fig. 2.3, we observe that the duty cycle, defined as the fraction of one period over which the function is non-zero, does not always coincide with the value of d, even though we call d the duty cycle parameter. When s is close to zero, so that the function is relatively square, the signal duty cycle is almost exactly equal to d. However, when s is significantly larger than zero, the signal becomes smoother, and its duty cycle can be more than the set value of d. This difference between the duty cycle and d is illustrated by the green curve in Fig. 2.3, for the case where $s = 0.3$. The inset in Fig. 2.3 shows the power spectrum for one of the square signals, with $s = 0$. As one expects, the power spectrum in this case contains many higher harmonics at significant amplitudes.

Three parameters are shown in Fig. 2.3 illustrating the effect of PPF, then in Fig. 2.3(a-b) the duty cycle (d) is altered from $d = 0.2$ to $d = 0.7$, which causes the graph to broaden horizontally while the location of the pulse (r) and the smoothness (s) are kept constant or fixed at $r = s = 0$. Then, in Fig. 2.3(c-d), the smoothness (s) is modified or changed from $d = 0.15$ to $d = 1.0$, which produces a perfect sine wave, while the two $d = 0.2$ to $d = 0.7$ of the pulse (r) and the duty cycle (d) are kept fixed at $r = 0$ and $d = 0.867$. Finally, in Fig. 2.3(f-e), we maintained two fixed parameters: duty cycle ($d = 0.05$) and smoothness ($s = 0$) and then changed the symmetry factor (r) from $r = 0$ (close to π) to $r = 0.8$, where the graph shift closed to zero. When you change by π and reflect 2π, the symmetry of translation is lost from shifting because now the pulse is getting close to zero,

As we have mentioned, for $d = s = 1$ the PPF approximates $\sin(t)$, which is convenient to make numerical comparisons with the case of harmonic driving. In our numerical implementation of the PPF (see Appendix A.2), we have used Levenberg-Marquart's least squares optimisation to obtain the best fit to $\sin(t)$. The optimised

parameters are $d = 0.8670$ and $s = 1$, giving a maximum difference between the two functions of less than 1.2×10^{-4}. These optimised parameters are set as the default values in our numerical implementation for convenience.

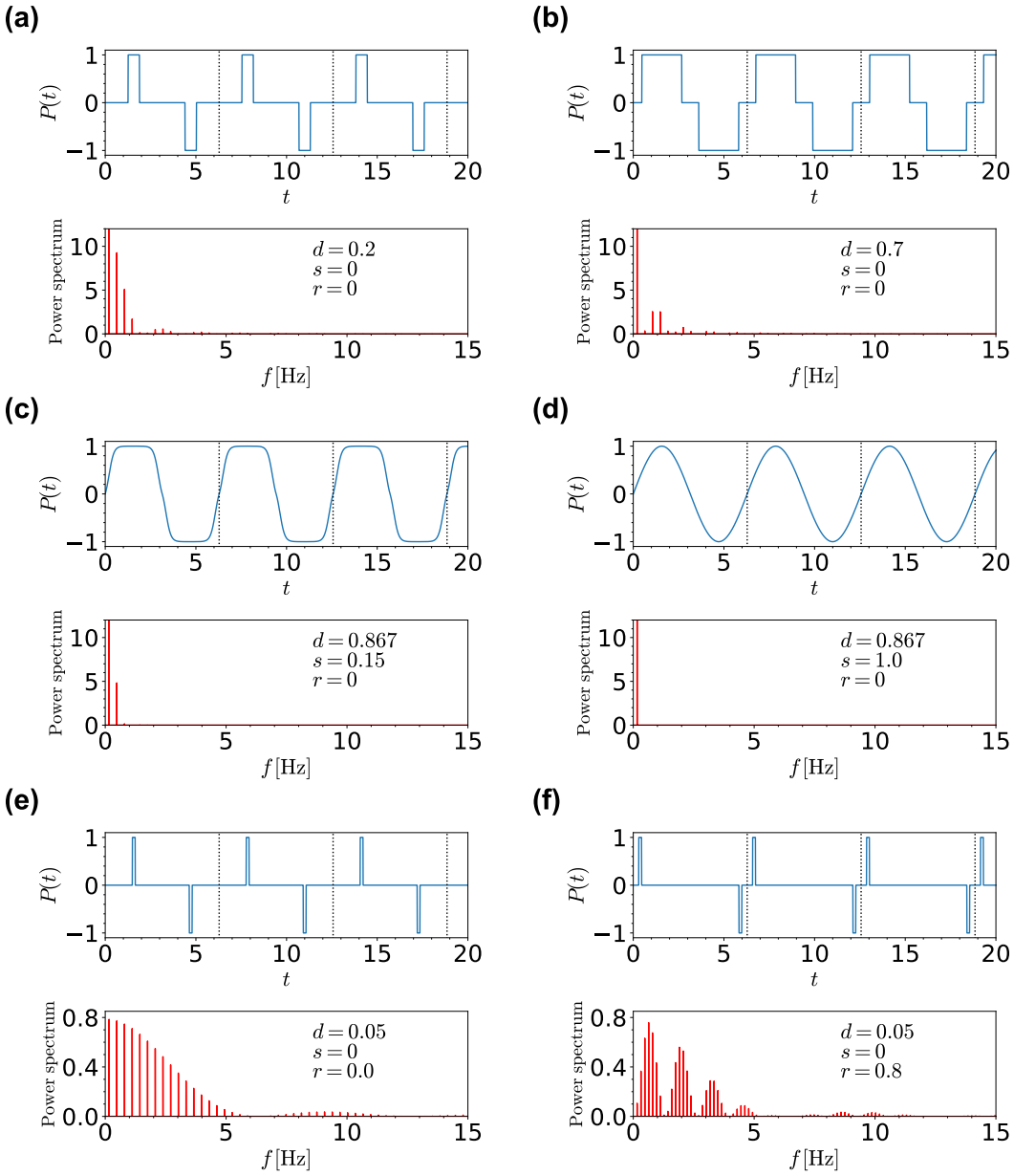


Figure 2.3: Four examples of the periodic pulse function, given by Eq. (2.29). A Black dashed line shows a square wave with a duty cycle of one. The blue dashed-dotted line shows, approximately, a sine wave. (c) The red line shows a square wave with a duty cycle of 0.2. (d) The green line shows a smooth waveform with a duty cycle that is also one, even though the duty cycle parameter is $d = 0.3$. The inset shows the power spectrum in the case of (c)

To obtain the derivative of the periodic pulse function (PPF), $P'(t)$, we first introduce compact notation for the two arguments of the exponential functions. Define

$$X_-(t) = |f(t)| - \beta - 1 + r(\beta - 1). \tag{2.33}$$

and

$$X_+(t) = |f(t)| + \beta - 1 + r(\beta - 1). \tag{2.34}$$

Using these definitions, the PPF from Eq. (2.29) can be written as

$$P(t) = \frac{\text{sign}(f(t))}{A}\left[A_0 + \frac{1}{1+\exp\left(\alpha X_-(t)\right)} - \frac{1}{1+\exp\left(\alpha X_+(t)\right)}\right]. \tag{2.35}$$

For $f(t) \neq 0$, the derivative of the absolute-value function is

$$\frac{d}{dt}|f(t)| = \text{sign}(f(t))f'(t). \tag{2.36}$$

And,

$$\frac{dX_-(t)}{dt} = \text{sign}(f(t))f'(t). \tag{2.37}$$

Similarly,

$$\frac{dX_+(t)}{dt} = \text{sign}(f(t))f'(t). \tag{2.38}$$

Hence,

$$X'_-(t) = X'_+(t) = \text{sign}(f(t))f'(t). \tag{2.39}$$

The derivative of the logistic-type function is

$$\frac{d}{dx}\left[\frac{1}{1+\exp(\alpha x)}\right] = -\frac{\alpha\exp(\alpha x)}{[1+\exp(\alpha x)]^2}. \tag{2.40}$$

Therefore,

$$\frac{d}{dt}\left[\frac{1}{1+\exp\left(\alpha X_{-}(t)\right)}\right] = -\frac{\alpha\exp\left(\alpha X_{-}(t)\right)}{\left[1+\exp\left(\alpha X_{-}(t)\right)\right]^{2}}\frac{dX_{-}(t)}{dt}. \tag{2.41}$$

Likewise,

$$\frac{d}{dt}\left[\frac{1}{1+\exp\left(\alpha X_{+}(t)\right)}\right] = -\frac{\alpha\exp\left(\alpha X_{+}(t)\right)}{\left[1+\exp\left(\alpha X_{+}(t)\right)\right]^{2}}\frac{dX_{+}(t)}{dt}. \tag{2.42}$$

Since A_0, A, and $\text{sign}(f(t))$ are constant with respect to t between zero crossings of $f(t)$,

$$\frac{dA_0}{dt} = 0, \qquad \frac{d}{dt}\,\text{sign}(f(t)) = 0, \qquad f(t) \neq 0. \tag{2.43}$$

Thus, differentiating Eq. (2.35) and applying the chain rule gives

$$\begin{aligned} P'(t) = \frac{\text{sign}(f(t))}{A}\Bigg[&- \frac{\alpha\exp\left(\alpha X_{-}(t)\right)}{\left[1+\exp\left(\alpha X_{-}(t)\right)\right]^{2}}\frac{dX_{-}(t)}{dt} \\ &+ \frac{\alpha\exp\left(\alpha X_{+}(t)\right)}{\left[1+\exp\left(\alpha X_{+}(t)\right)\right]^{2}}\frac{dX_{+}(t)}{dt}\Bigg]. \end{aligned} \tag{2.44}$$

Substituting the derivatives of $X_{-}(t)$ and $X_{+}(t)$ gives

$$\begin{aligned} P'(t) = \frac{\text{sign}(f(t))}{A}\Bigg[&- \frac{\alpha\exp\left(\alpha X_{-}(t)\right)}{\left[1+\exp\left(\alpha X_{-}(t)\right)\right]^{2}}\text{sign}(f(t))f'(t) \\ &+ \frac{\alpha\exp\left(\alpha X_{+}(t)\right)}{\left[1+\exp\left(\alpha X_{+}(t)\right)\right]^{2}}\text{sign}(f(t))f'(t)\Bigg]. \end{aligned} \tag{2.45}$$

Since

$$\text{sign}^2(f(t)) = 1, \qquad f(t) \neq 0, \tag{2.46}$$

The derivative reduces to

$$P'(t) = \frac{\alpha f'(t)}{A}\left[\frac{\exp\left(\alpha X_{+}(t)\right)}{\left[1+\exp\left(\alpha X_{+}(t)\right)\right]^{2}} - \frac{\exp\left(\alpha X_{-}(t)\right)}{\left[1+\exp\left(\alpha X_{-}(t)\right)\right]^{2}}\right]. \tag{2.47}$$

The sawtooth function in Eq. (2.32) away from its discontinuities, its derivative is

$$f'(t) = -\frac{2}{\pi}. \tag{2.48}$$

Hence,

$$P'(t) = -\frac{2\alpha}{A\pi}\left[\frac{\exp\left(\alpha X_+(t)\right)}{\left[1+\exp\left(\alpha X_+(t)\right)\right]^2} - \frac{\exp\left(\alpha X_-(t)\right)}{\left[1+\exp\left(\alpha X_-(t)\right)\right]^2}\right]. \tag{2.49}$$

For numerical stability, we use

$$\frac{\exp(x)}{\left[1+\exp(x)\right]^2} = \frac{1}{\left[\sqrt{\exp(-x)}+\sqrt{\exp(x)}\right]^2}. \tag{2.50}$$

Thus,

$$\frac{\exp\left(\alpha X_+(t)\right)}{\left[1+\exp\left(\alpha X_+(t)\right)\right]^2} = \frac{1}{\left[\sqrt{\exp\left(-\alpha X_+(t)\right)}+\sqrt{\exp\left(\alpha X_+(t)\right)}\right]^2}. \tag{2.51}$$

Similarly,

$$\frac{\exp\left(\alpha X_-(t)\right)}{\left[1+\exp\left(\alpha X_-(t)\right)\right]^2} = \frac{1}{\left[\sqrt{\exp\left(-\alpha X_-(t)\right)}+\sqrt{\exp\left(\alpha X_-(t)\right)}\right]^2}. \tag{2.52}$$

Therefore,

$$\begin{aligned} P'(t) = -\frac{2\alpha}{A\pi}\Bigg[&\frac{1}{\left[\sqrt{\exp\left(-\alpha X_+(t)\right)}+\sqrt{\exp\left(\alpha X_+(t)\right)}\right]^2} \\ &- \frac{1}{\left[\sqrt{\exp\left(-\alpha X_-(t)\right)}+\sqrt{\exp\left(\alpha X_-(t)\right)}\right]^2}\Bigg]. \end{aligned} \tag{2.53}$$

Let

$$p(t) = \alpha \Bigg[\frac{1}{\left[\sqrt{\exp\left(-\alpha X_+(t)\right)} + \sqrt{\exp\left(\alpha X_+(t)\right)} \right]^2} - \frac{1}{\left[\sqrt{\exp\left(-\alpha X_-(t)\right)} + \sqrt{\exp\left(\alpha X_-(t)\right)} \right]^2} \Bigg]. \tag{2.54}$$

The derivative therefore takes the same compact form as used in the implementation of `dppf()`:

$$P'(t) = -\frac{2p(t)}{A\pi}, \tag{2.55}$$

c.f. Appendix A.2.

Chapter 3

Phase Control of Chaos in the Duffing System

3.1 Introduction

This chapter systematically investigates the phase control of chaos in the Duffing system under anharmonic excitation. By anharmonic excitation, we mean a periodic excitation that includes the fundamental (harmonic) plus higher harmonics with non-trivial amplitudes. Our literature review indicates that most nonlinear systems have been controlled only by simple harmonic signals, leaving the unexplored question of how the presence of higher harmonics in the drive signal affects phase control of chaos.

More generally, this chapter addresses an often-overlooked aspect of phase control of chaos, namely that the method does not actually reduce the amount of chaos in the parameter space, but rather shifts it from one area to another. Evidence of this behaviour can be seen in the results reported by Martinez et al. [25, 26], which will serve as an important reference throughout this chapter. As we shall see, the phase control of chaos strategy can convert chaotic motion into quasi-periodic or periodic motion at specific parameter values, but this does not necessarily reduce the total amount of chaos in the system's parameter space. In most cases, applying the control signal simply redistributes the regular and chaotic regions in parameter space. In the following results, we investigate this question in detail.

3.2 Results

To solve the Duffing system (Eq. (1.2)), we use the `DOP853` solver from `scipy.integrate` with the absolute and relative error tolerances both set equal to 1×10^{-10}. To begin with, we reproduce the results given in Fig. 4 of Ref. [25]. Figure 3.1(a) shows a high-resolution view of the maximal Lyapunov exponent for the case $m = 0$.

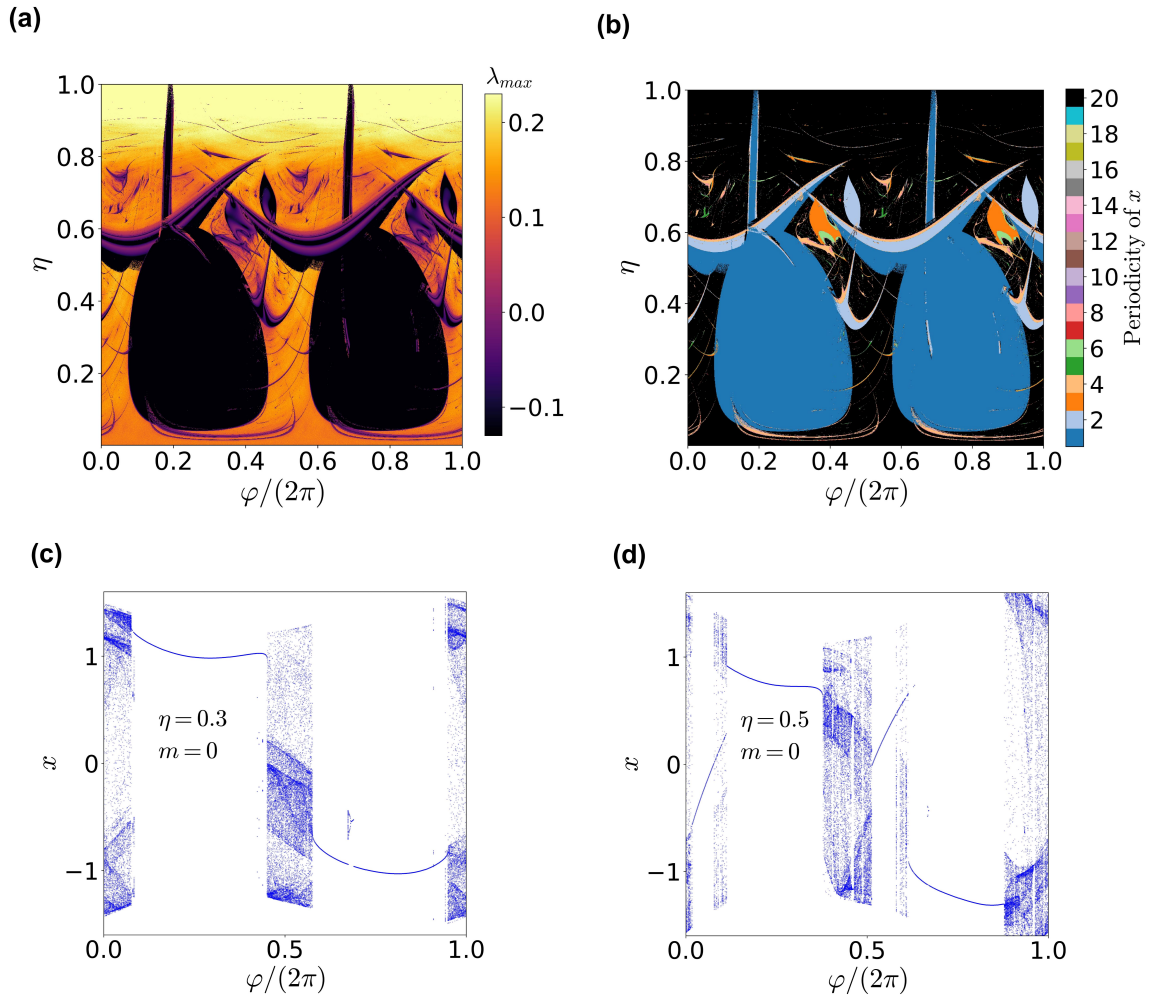


Figure 3.1: (a) Present the numerically maximal Lyapunov exponent diagrams in the $\varphi - \eta$ control plane for the shape parameter $m = 0$ (sinusoidal wave), where λ_{max} derived from Eq. (2.18). (b) Show the corresponding 2-dimensional periodogram for numerically calculated regularisation regions in the $\varphi - \eta$ control plane for the shape parameter $m = 0$ (sinusoidal wave), using the PPF and its derivative given by Eq. (2.29) and Eq. (2.53). (c), and (d) demonstrate 1-dimensional bifurcation diagrams when changing the control $\eta = 0.3$ and $\eta = 0.5$, constructing the 2-dimensional periodogram in (b). Fixed parameters: $\delta = 0.25, \beta = 1, \gamma = 0.29$, and $\omega = 1$.

Martinez et al. [25] demonstrated that the non-chaotic regions seen in Fig. 3.1(a) coincide with the numerically calculated regularisation regions (see, for example, Fig. 5 of Ref. [25]). To see this more clearly, we have recalculated the regularisation regions corresponding to Fig. 3.1(a) using the periodic pulse function (PPF) method. The result is shown in Fig. 3.1(b), and the 1-dimensional bifurcation diagrams shown in Fig. 3.1(c) and 3.1(d) for representative values of the control amplitude $\eta = 0.3$ and $\eta = 0.5$ reveal the underlying periodic windows and bifurcation structures that collectively generate the regularisation regions observed in the parameter space of Fig. 3.1(b). Comparison of Fig. 3.1(a) and Fig. 3.1(b) shows that the maximal Lyapunov exponent for the case $m = 0$ gives more similar or less exact results, such as periodicity, which means that we don't always have to calculate the Lyapunov exponent because it is easier to calculate the periodicity.

To understand Fig. 3.1(b) clearly, we analyse 1-dimensional diagrams in Fig. 3.1(c,d), which illustrate that a system is chaotic when the amplitude of the control signal $\varphi/2\pi = 0$ or close to zero, which implies that no control is applied; each time you sample the signal $\varphi/2\pi$ at different values of x, you get the spread of points in the Poincaré section, which shows chaotic behaviour. By increasing $\varphi/2\pi$ in Fig. 3.1(c) from 0.1 to 0.47, the system transitions from chaos to period 1 (counting the number of lines within periodic windows), then increasing $\varphi/2\pi$ further, we see that chaos occurs again from $\varphi/2\pi = 0.47$ to 0.59, then increasing $\varphi/2\pi$ more further, we see a transition to period 1 from $\varphi/2\pi = 0.6$ to 0.9, then increasing $\varphi/2\pi$ chaos occurs again from $\varphi/2\pi = 0.9$ to 1.0. Therefore, in Fig. 3.1(d), we see the same transition from chaos to period 1 then chaos, but in a different control $\varphi/2\pi$ compared to Fig. 3.1(c), and we observe more chaos when $\eta = 0.5$ than $\eta = 0.3$ in a parameter space. This is what they show in the work of Martinez et al. [25] when they control chaos.

Secondly, we reproduced the findings given in Fig. B1 of Ref. [26]. Fig. 3.2(a,b), the top panels show a 1-dimensional bifurcation diagram for two cases $m = 0$ and $m = 0.95$. In Fig. 3.2(a), it shows that the system is chaotic when the amplitude of the control signal $\eta = 0$ or η is close to zero (no control). When applying the control by increasing η to 0.1, the system transitions from chaos to period 3; then increasing η further, we see chaos from $\eta = 0.2$ to 0.5; then increasing η further again, we see a transition to period 3 from 0.6 to 0.7; then increasing η, we see chaos occurs from 0.8 to 1.0. Therefore, in Fig. 3.2(b), we see the same transition from chaos to period 3 then chaos, but in a different control amplitude η compared to Fig. 3.2(b), and we observe extra periodic windows when $m = 0.95$ from $\eta = 0.24$ to 0.42 compared to $m = 0$, where we see chaos, but no overall chaos reduction in parameter space. However, in Fig. 3.2(c,d), the

bottom panels show the corresponding harmonic drive (f(t)) for the elliptic function, where the shape parameter is increased from Fig. 3.2(c) $m = 0$ (sinusoidal wave) to Fig. 3.2(d) $m = 0.95$ (double-humped wave), and both apply the same initial conditions following the attractor for the range of η values. This is what they show in the work of Martinez et al. [26] when they control chaos.

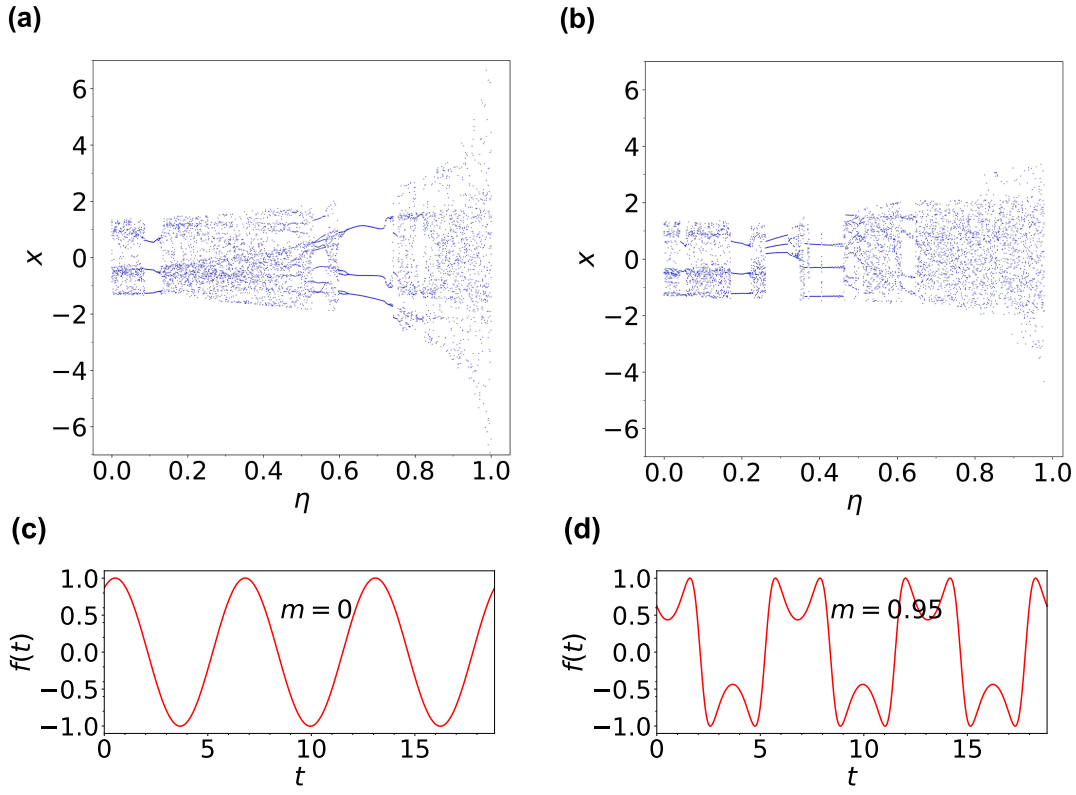


Figure 3.2: (a,b) The top panels present the 1-dimensional bifurcation diagrams for the function of the amplitude of the control signal η and variable x corresponding to Eq. (1.1), with the corresponding harmonic drive (f(t)) for the elliptic function. The blue lines show the periodic windows of period 3, and the blue dotted region represents chaos. (c) The bottom panels show the drive signal where the shape parameter $m = 0$ (sinusoidal wave), which is varied with (d) $m = 0.95$ (double-humped wave). Fixed parameters: $\delta = 0.25, \sigma = 0, \beta = 1, \gamma = 0.29, \phi = \frac{\pi}{3}, \frac{F_{i-1}}{F_L} = \frac{2}{3}$, and $\omega = 1$.

On the other hand, our approach aims to determine whether it is possible to apply a control signal to the system to reduce the overall amount of chaos in the system's parameter space. We begin by replacing the control signal elliptic function used by Martinez et al. [26] in Fig. 3.2(a,b) with the periodic pulse function (PPF) given by Eq. (2.29). This pulse allows for further tuning using the duty cycle (d), smoothness (s), and the symmetry factor (r), which play a crucial role in chaos suppression. In

Fig. 3.3(a,b), we vary the duty cycle $d = 0.4$ and $d = 0.6$ while fixing the smoothness $s = 0$, the symmetry factor $r = 0$ and the phase $\varphi = \pi/3$.

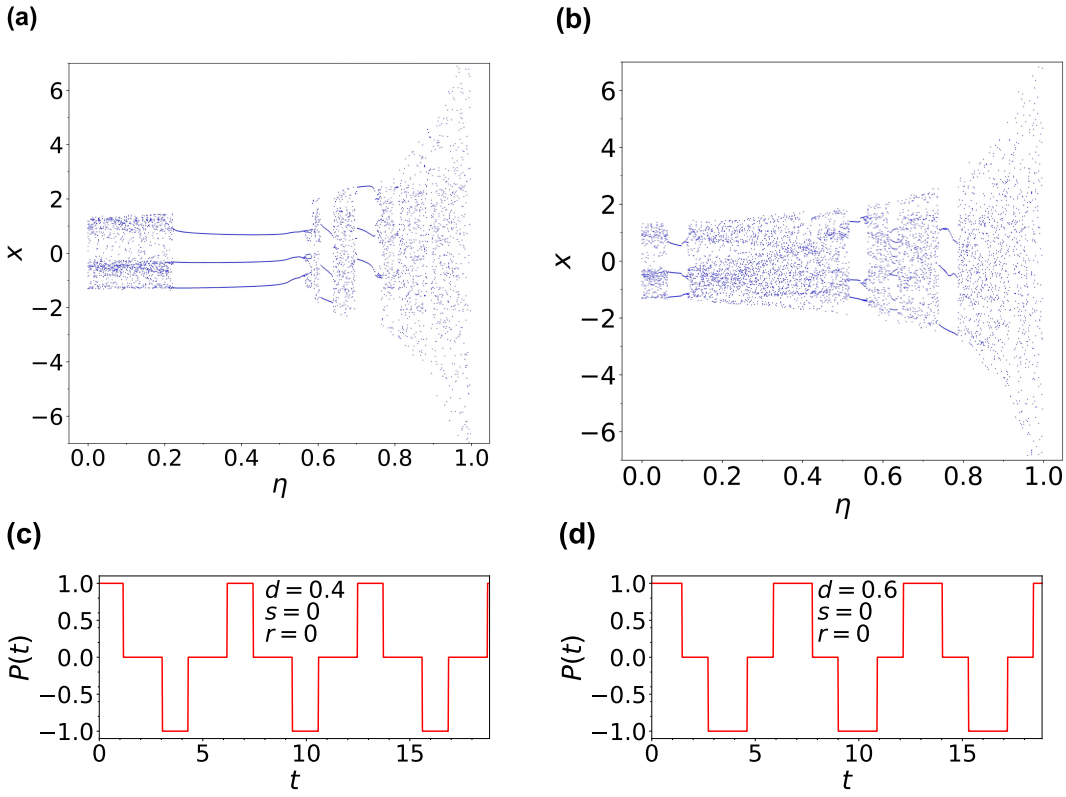


Figure 3.3: (a,b) The top panels present 1-dimensional bifurcation diagrams for the function of the amplitude of the control signal η and variable x corresponding to Eq. (2.29) with the corresponding anharmonic drive (P(t)) for the periodic pulse function. While varying the duty cycle (c) $d = 0.4$ and (d) $d = 0.6$. The bottom panels show the drive signal, where the smoothness parameters are the same: $s = 0$ (square wave). Fixed parameters: $(s = 0, r = 0, \delta = 0.25, \sigma = 0, \beta = 1, \gamma = 0.29, \phi = \frac{\pi}{3}, \frac{F_{i-1}}{F_L} = \frac{2}{3}$, and $\omega = 1)$

When we apply the periodic pulse function control signal to the top panel in Fig. 3.3(a), where the duty cycle $d = 0.4$, then between $\eta = 0.22$ and $\eta = 0.58$, we get much wider periodic windows than what we get with the elliptic function control signal in Fig. 3.2(a) (top panel). Then, in Fig. 3.3(b) (top panel), we increase the duty cycle to $d = 0.6$, and then between $\eta = 0.06$ and $\eta = 0.14$, we get much narrower periodic windows than what we get with the elliptic function control signal in Fig. 3.2(a) (top panel). The bottom panels in Fig. 3.3(c,d) show the anharmonic drive (P(t)) for the periodic pulse function, where the smoothness parameters are the same, $s = 0$ (square wave).

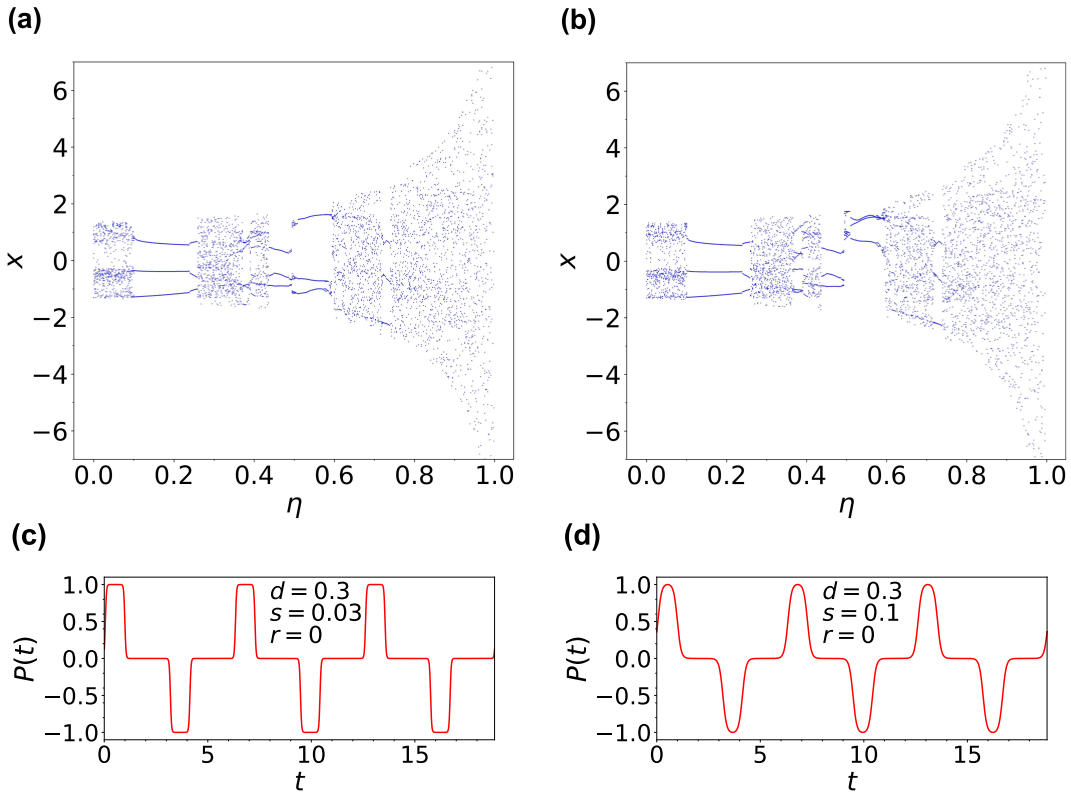


Figure 3.4: (a,b) The top panels present the 1-dimensional bifurcation diagrams for the function of the amplitude of the control signal η and variable x corresponding to Eq. (2.29), with the corresponding anharmonic drive (P(t)) for the periodic pulse function. While varying the smoothness, (c) $s = 0.03$ and (d) $s = 0.1$. (c) The bottom panels show the drive signal, where the smoothness $s = 0.03$ (smooth square wave) is varied with (d) $s = 0.1$ (round square wave). Fixed parameters: $(d = 0.3, r = 0, \delta = 0.25, \sigma = 0, \beta = 1, \gamma = 0.29, \phi = \frac{\pi}{3}, \frac{F_{i-1}}{F_L} = \frac{2}{3}$, and $\omega = 1)$

In Fig. 3.4(a,b), we vary the smoothness $s = 0.03$ and $s = 0.1$ while fixing the duty cycle $d = 0.3$, the symmetry factor $r = 0$ and the phase shift $\varphi = \pi/3$. When we apply the periodic pulse function control signal to the top panel in Fig. 3.4(a), where $s = 0.03$, we get substantially wider periodic windows between $\eta = 0.1$ and $\eta = 0.3$, and a mirrored (extra) period 3 where $\eta = 0.5$ between $\eta = 0.43$ and $\eta = 6$. In Fig. 3.4(b) (top panel), we increase the smoothness $s = 0.1$, then we get the same result, except for period 2 in $\eta = 0.5$ to $\eta = 0.6$ rather than period 3 as shown in Fig. 3.4(a). The bottom panels show the anharmonic drive (P(t)) for the periodic pulse function, where the smoothness parameter in Fig. 3.4(c) $s = 0.03$ (smooth square wave), is varied to Fig. 3.4(d) $s = 0.1$ (round square wave). As a result of the nonlinear system locking its frequency to the drive signal, we obtain periodic windows due to chaos control (the

system becomes regular because of locks).

The 1-dimensional bifurcation diagram in Fig. 3.4(a,b) clearly shows periodic and chaotic regions, but since it is limited to a single parameter slice, it cannot reveal how these dynamical behaviours are organised throughout the entire parameter space. We will therefore extend the analysis in the next section to a 2-dimensional periodogram shown in Fig. 3.5 by writing a Python script that stores the values of x (producing a file that contains all the values of x) for given values of η. Then we examine how many unique values of x are associated with particular values of η, which are three values called the period 3. As a result, we can find periodicity as a function of η; we do so not only at one parameter but also with the change parameter so that we can plot the second parameter in the direction of y. Therefore, we can do this for any set of parameters in Fig. 3.3 or Fig. 3.4, and in Fig. 3.5, we determine the periodicity as a function of two of the parameters to generate the 2-dimensional periodograms.

Section 3.3 presents the results of the Gamma (γ) versus Beta (β) plane, followed by a detailed Table 3.1, Table 3.2, Table 3.3 and Table 3.4 with a comparison summary (Subsection 3.3.1). Section 3.4 shows the results of the Delta (δ) versus Gamma (γ) plane, and Subsection 3.4.1 presents comparison summary with Table 3.5, Table 3.6, Table 3.7, and Table 3.8.

3.3 Results of Gamma (γ) versus Beta (β) plane

This section presents the results obtained by changing the damping coefficient (γ) and the nonlinear stiffness parameter (β), along with a comparison of the control signals used to suppress chaos. We first consider the elliptic function control signal given by Eq. (1.1) following the approach of Martinez et al. [25, 26]. This control signal is characterised by the control amplitude ($\eta \in [0, 1]$), phase shift ($\varphi \in [0, \pi]$), control frequency ($\omega \in 0.5, 1.0$), and shape parameter (m), where $m = 0$ is a sinusoidal waveform, $m = 0.717 \simeq m_{max}^{impulse}$ is a nearly square wave and $m = 0.9999$ is a double-humped waveform. The other system parameters are fixed at $\gamma = 0.29$, $\delta = 0.25$, and $\beta = 1.0$. Then we replace the excitation of the elliptic function with a periodic pulse function (PPF) defined by Eq. (2.29), which allows for more control through the duty cycle (d), smoothness (s) and the symmetry factor (r).

To evaluate the effectiveness of two distinct control signals, we first set up a reference case by examining both an uncontrolled system ($\eta = 0$) and a weakly controlled system

($\eta = 0.03$). In these comparisons, the phase shift and the control frequency are kept at $\varphi = p = \pi/2$ and $\omega = 0.5$, while changing the shape parameters $m = 0$, 0.717 and 0.9999 for the elliptic excitation, and using values of $s = 0$, 0.717 and 0.9999 for PPF, keeping $d = 0.05$ and $r = 0$. After this baseline behaviour is established, stronger cases are explored by increasing the control amplitude to $\eta = 0.30$ and 0.60, while fixing the parameters at $\varphi = p = 0.85$, $\omega = 1.0$, $m = 0.02$, $s = 0.02$, $d = 0.5$ and $r = 0.01$. In this chapter, when the periodicity of x exceeds 20, the system is considered chaotic. The variable C represents the fraction of the chaotic parameter space and is determined as the ratio of the black area (periodicity > 20) to the total area in the periodogram.

In Fig. 3.5(a,b), the upper panels show the baseline 2-dimensional periodograms for the elliptic function and the periodic pulse function (PPF) before any control is applied ($\eta = 0$). The two systems correspond to the uncontrolled case and therefore

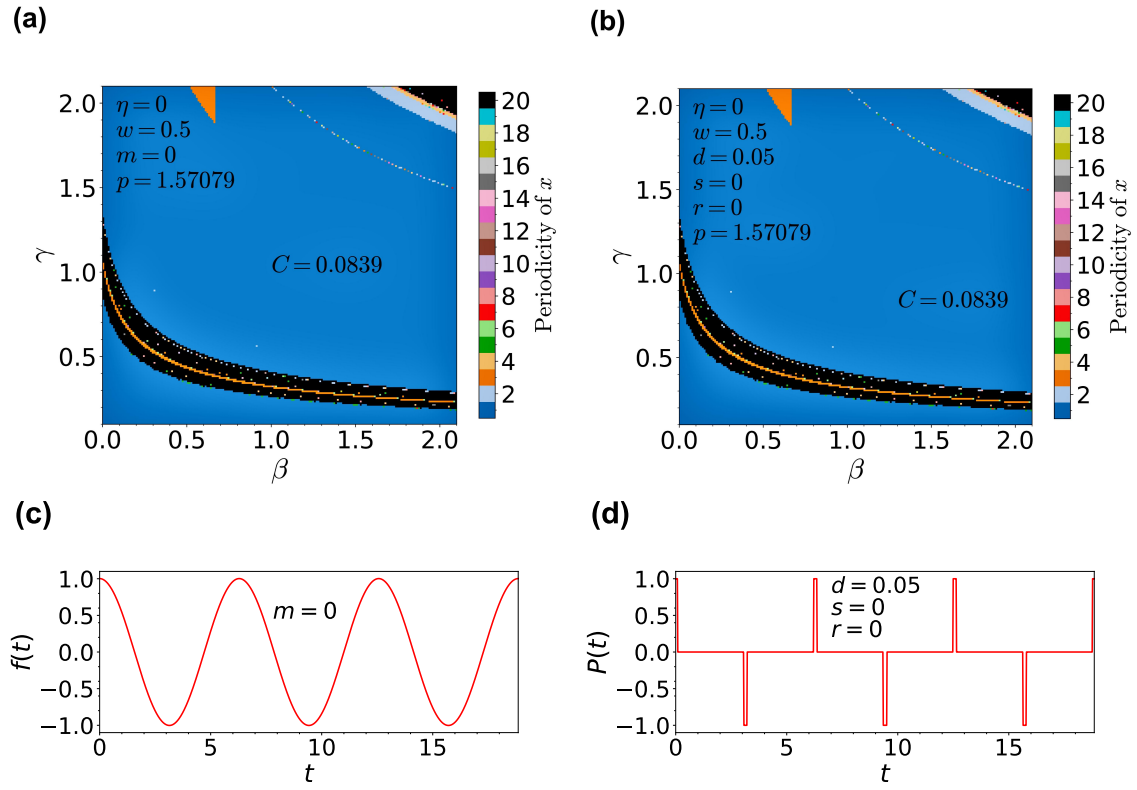


Figure 3.5: (a) and (b) show the results, where the top panels present a 2-dimensional periodogram baseline comparison between the elliptic function and periodic pulse function (PPF), when no control $\eta = 0$ is applied. Lower panels demonstrate corresponding excitation waveforms: (c) elliptic function ($f(t)$) with $m = 0$ sinusoidal waveform, and (d) PPF ($P(t)$) with $s = 0$ square wave-like waveform. Fixed parameters: $\omega = 0.5$, $p = 1.57079$, $d = 0.05$, and $r = 0$.

produce identical parameter-space structures with $C = 0.0839$. The colours indicate the periodicity of x, while the black regions correspond to periodicities greater than 20 and are therefore classified as chaotic. The lower panels show the corresponding excitation waveforms. Fig. 3.5(c) gives the elliptic excitation for $m = 0$, which reduces to a sinusoidal waveform; Fig. 3.5(d) gives the PPF excitation for $s = 0$ corresponding to the square wave with fixed duty cycle $d = 0.05$ and symmetry factor $r = 0$. These uncontrolled periodograms will serve as the reference state against which the effectiveness of subsequent control signals will be measured.

In Fig. 3.6(a,b), a weak control signal of amplitude $\eta = 0.03$ is applied without changing the shape parameters $m = 0$ for the elliptical function and $s = 0$ for PPF. A

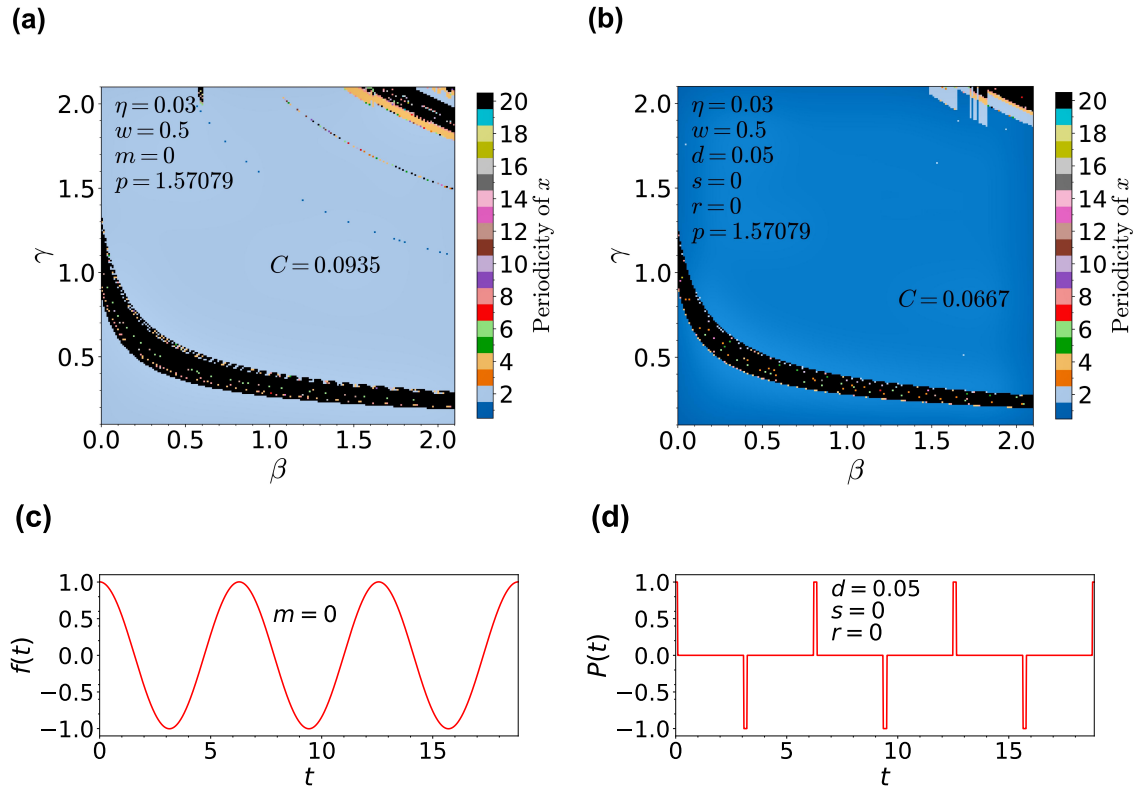


Figure 3.6: (a) and (b) present the results, where the top panels demonstrate 2-dimensional periodograms for baseline comparison between the elliptic function and periodic pulse function (PPF), when control amplitude $\eta = 0.03$ is applied. The lower panels present corresponding excitation waveforms: (c) elliptic function ($f(t)$) with $m = 0$ sinusoidal waveform and (d) PPF ($P(t)$) with $s = 0$ square wave-like waveform. Fixed parameters: $\omega = 0.5$, $p = 1.57079$, $d = 0.05$, and $r = 0$.

comparison between Fig. 3.6(a) and the baseline in Fig. 3.5(a) shows that the chaotic fraction increases from $C = 0.0839$ to $C = 0.0935$; this indicates that the application of

a sinusoidal elliptic control signal has slightly enlarged the chaotic region in parameter space. In contrast, as seen in Fig. 3.6(b), because it gives $C = 0.0667$, which is less than the baseline value $C = 0.0839$, one could say that square-wave-like PPF excitation reduces the chaotic area. Differences are most visible in black regions near the upper right corner of the periodogram, along a curved band extended from $y = 1.0$. The waveforms in Fig. 3.6(c,d) are identical to those in Fig. 3.5(c,d), with only the control amplitude modified.

In Fig. 3.7(a,b), we maintain the control amplitude at $\eta = 0.03$, as in Fig. 3.6(a,b); however, we change the shape parameters from $m = 0$ to $m = 0.717$ for the elliptic function and from $s = 0$ to $s = 0.717$ for PPF. When comparing the top panels, we see

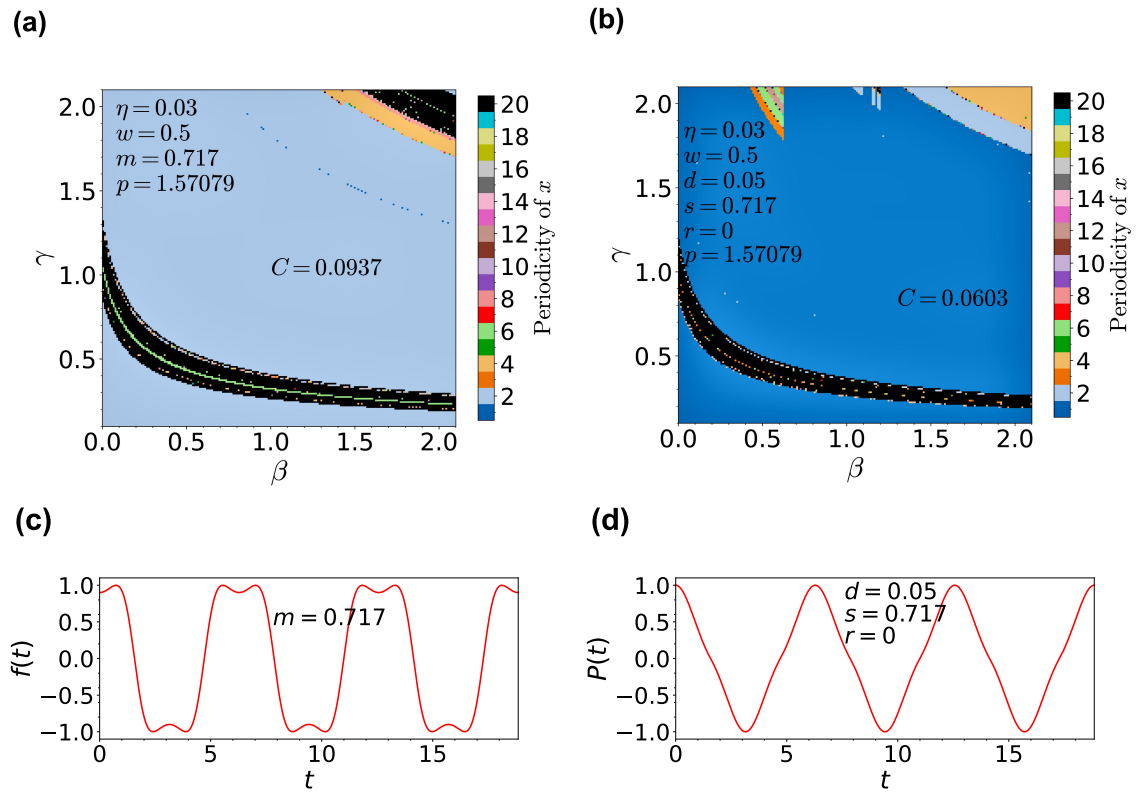


Figure 3.7: (a) and (b) demonstrate the results, where the top panels present 2-dimensional periodograms for both elliptic and periodic pulse functions when control signal $\eta = 0.03$ is applied, then the bottom panels show the corresponding drive signals for the elliptic function (f(t)) using shape parameter $m = 0.717$ (Nearly square wave) and the periodic pulse function (P(t)) using smoothness parameter $s = 0.717$ (Nearly sinusoidal wave). Fixed parameters: $w = 0.5$, $p = 1.57079$, $d = 0.05$, and $r = 0$.

that $C = 0.0937$ in Fig. 3.7(a) is marginally greater than $C = 0.0935$ in Fig. 3.6(a). This number is larger than the uncontrolled baseline value of C, which is 0.0839, as

illustrated in Fig. 3.5(a). In contrast, Fig. 3.7(b) provides $C = 0.0603$, which is lower than what we found before in Fig. 3.6(b) ($C = 0.0667$) and the baseline uncontrolled condition in Fig. 3.5(b). This decrease presents itself as smaller black chaotic regions, most notably in the upper-right portion of parameter space, as well as a curving band extended from $y = 1.0$ to more negative values on the y-axis. The appropriate drive signals are presented in the panels below. The elliptic function drive for $m = 0.717$, shown in Fig. 3.7(c), results in a nearly square-wave excitation, but the PPF waveform for $s = 0.717$, shown in Fig. 3.7(d), has a nearly sinusoidal wave-like shape.

In Fig. 3.8(a,b), we maintain the control amplitude at $\eta = 0.03$, as in Fig. 3.7(a,b) and Fig. 3.6(a,b), while the shape parameter is increased from $m = 0.717$ to $m = 0.9999$ for the elliptic function and from $s = 0.717$ to $s = 0.9999$ for the periodic pulse function (PPF). The top panel shows that Fig. 3.8(a) gives a value of $C = 0.0824$, which is less

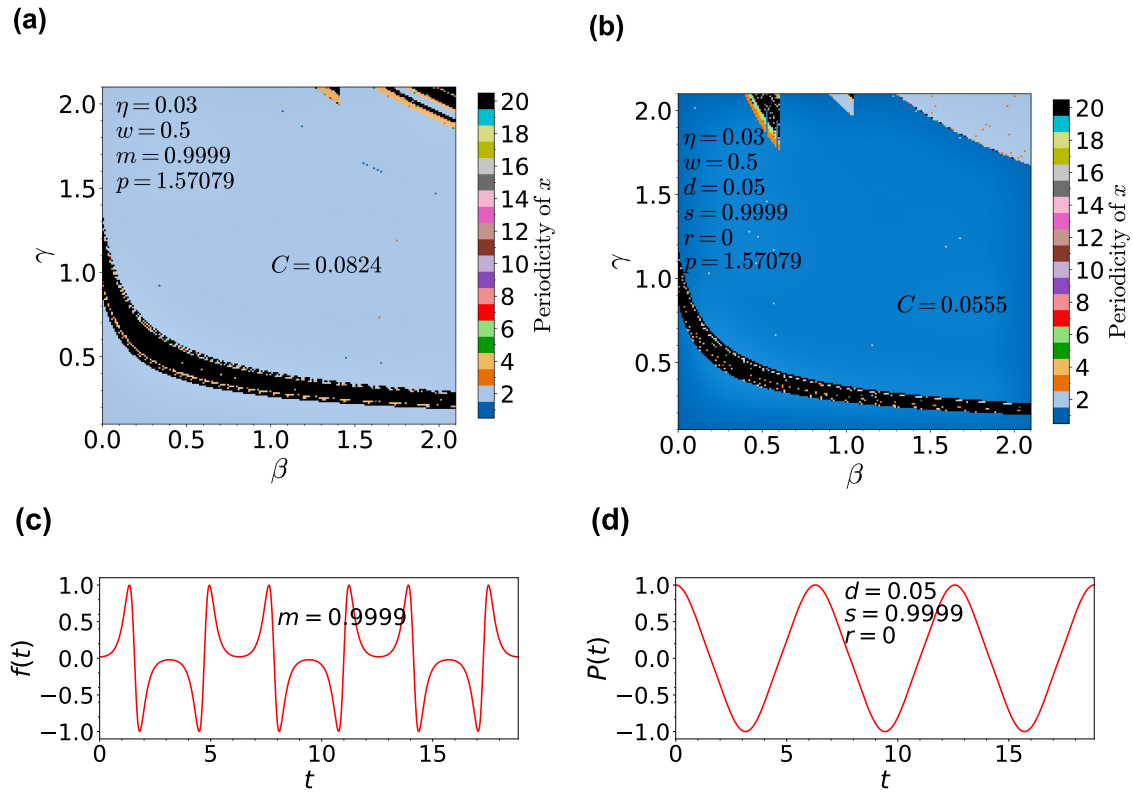


Figure 3.8: (a) and (b) show the results, where the top panels present 2-dimensional periodograms for both elliptic and periodic pulse functions when control signal $\eta = 0.03$ is applied; then the bottom panels show the corresponding drive signals for the elliptic function (f(t)) using shape parameter $m = 0.9999$ (double-humped wave) and the periodic pulse function (P(t)) using smoothness parameter $s = 0.9999$ (smooth sinusoidal wave). Fixed parameters: $\omega = 0.5$, $p = 1.57079$, $d = 0.05$, and $r = 0$.

than those found in Fig. 3.7(a) ($C = 0.0937$) and Fig. 3.6(a) ($C = 0.0935$); it is also slightly less than the uncontrolled baseline with $C = 0.0839$ shown in Fig. 3.5(a). This result means that with the double-humped elliptic waveform, there is a small reduction of the chaotic area compared to both the baseline and previous elliptic-control cases. Similarly, Fig. 3.8(b) yields $C = 0.0555$, which is less than the results of Fig. 3.7(b), Fig. 3.6(b) and the uncontrolled baseline in Fig. 3.5(b). In this instance, both control signals reduce chaos, but PPF does so much more successfully than the elliptic function. This is demonstrated by the further shrinkage of the black chaotic regions, especially from the upper right corner and along the curved chaotic band extended from $y = 1.0$. The bottom panels show the corresponding drive signals; Fig. 3.8(c) has the excitation by an elliptic function for $m = 0.9999$, thus giving a double-humped waveform, while Fig. 3.8(d) shows a PPF waveform when $s = 0.9999$, giving a smooth sinusoidal profile.

After looking at weak-control cases with $\eta = 0.03$, we now move to strong control amplitudes of $\eta = 0.30$ and $\eta = 0.60$ to test how well the elliptic function and the PPF work in reducing chaos within the (γ, β) parameter space plane with fixed parameters: $m = 0.02$, $s = 0.02$, $d = 0.5$, $r = 0.01$, $p = 0.85$ and $\omega = 1$. Note that the uncontrolled case, where $\eta = 0$, remains the same for all shape parameters because no control signal is applied. Therefore, the baseline value of $C = 0.0839$ does not change through this analysis.

In Fig. 3.9(a), the elliptic function produces a value of $C = 0.1001$, which is higher than the uncontrolled baseline value of $C = 0.0839$ from Fig. 3.5(a). This indicates that as the parameter increases, the chaotic region expands. By contrast, in Fig. 3.9(b) the same parameter yields $C = 0.0279$ for PPF, which is much less than its baseline value; here we notice huge shrinkage of black chaotic regions, particularly within the upper right corner and along that curved chaotic band starting from $y = 1.0$. The elliptic function control increases chaotic behaviour for the set parameters, while PPF has a very significant suppression effect. The bottom panels show the corresponding drive signals. Fig. 3.9(c) presents essentially sinusoidal elliptic function excitation for $m = 0.02$, while Fig. 3.9(d) gives a smooth square-wave-like PPF waveform at $s = 0.02$. It can be concluded from these results that waveform shape has an essential influence on chaos suppression efficiency.

In Fig. 3.10(a,b), the control amplitude increases from $\eta = 0.30$ to $\eta = 0.60$, while all other parameters remain constant. A comparison of the top panels shows that Fig. 3.10(a) gives $C = 0.0967$, which is slightly less than that obtained in Fig. 3.9(a), which was $C = 0.1001$, but still more than the uncontrolled baseline value $C = 0.0839$.

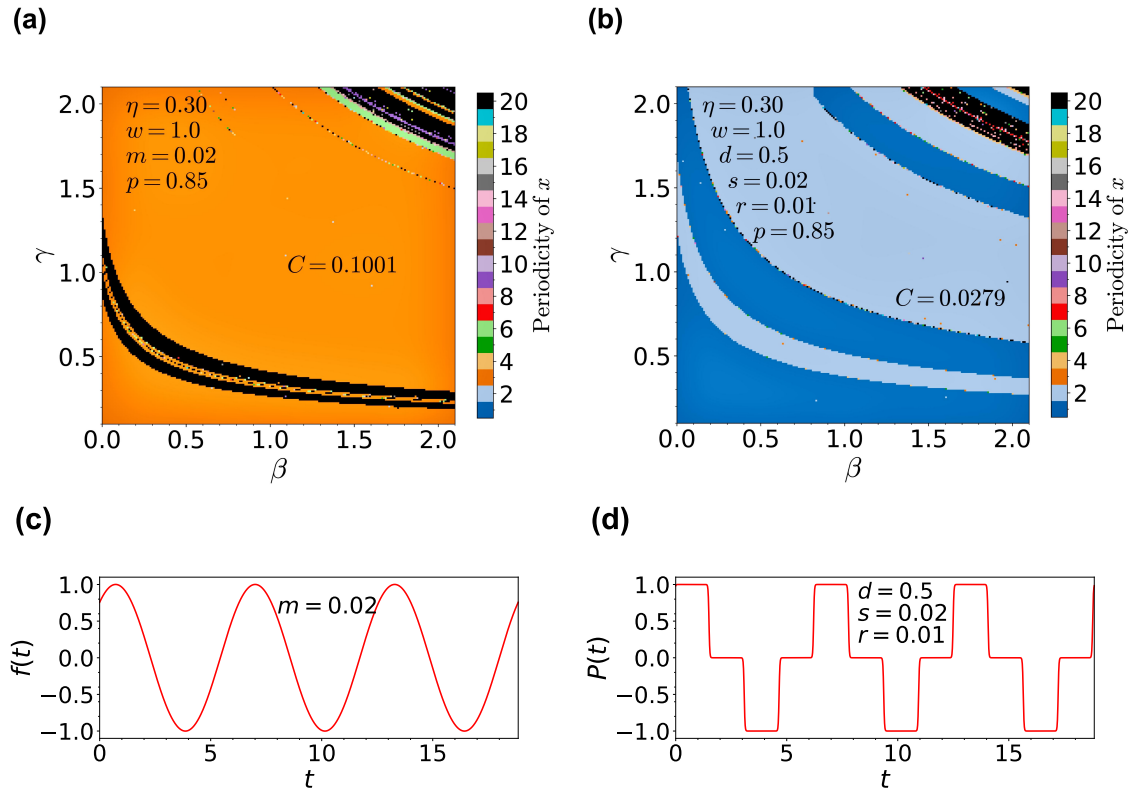


Figure 3.9: (a) and (b) present the 2-dimensional periodograms for the elliptic function and the periodic pulse function (PPF), respectively, with control amplitude fixed at $\eta = 0.30$. Bottom panels show corresponding drive signals: (c) elliptic function excitation $f(t)$ for $m = 0.02$, which is sinusoidal, and (d) periodic pulse function $P(t)$ for $s = 0.02$ resembling a smooth square wave. Fixed parameters are $\omega = 1.0$, $p = 0.85$, $d = 0.5$, and $r = 0.01$.

Therefore, increasing the control amplitude slightly reduces the chaos area compared to the case of $\eta = 0.30$, although the elliptic function control produces more chaos than an uncontrolled system. On the other hand, Fig. 3.10(b) gives a value of $C = 0.0001$, which is significantly lower than both Fig. 3.9(b) ($C = 0.0279$) and the uncontrolled baseline $C = 0.0839$ (The black region in the upper right corner is almost eliminated, and the one curving from $y = 1.0$ is eliminated for PPF but is drastically changed for the elliptic function). Therefore, in Fig. 3.10(a), chaos increases, but in Fig. 3.10(b), chaos decreases. The bottom panels in Fig. 3.10(d) give the same drive signal for the elliptic function (Sinusoidal wave) in Fig. 3.10(c) and the periodic pulse function (Smooth square wave) in Fig. 3.10(d), identical to Fig. 3.9(a,b), because the shape parameter (m) and smoothness (s) did not change.

The results presented in Fig. 3.5–3.10 show that chaos suppression is strongly de-

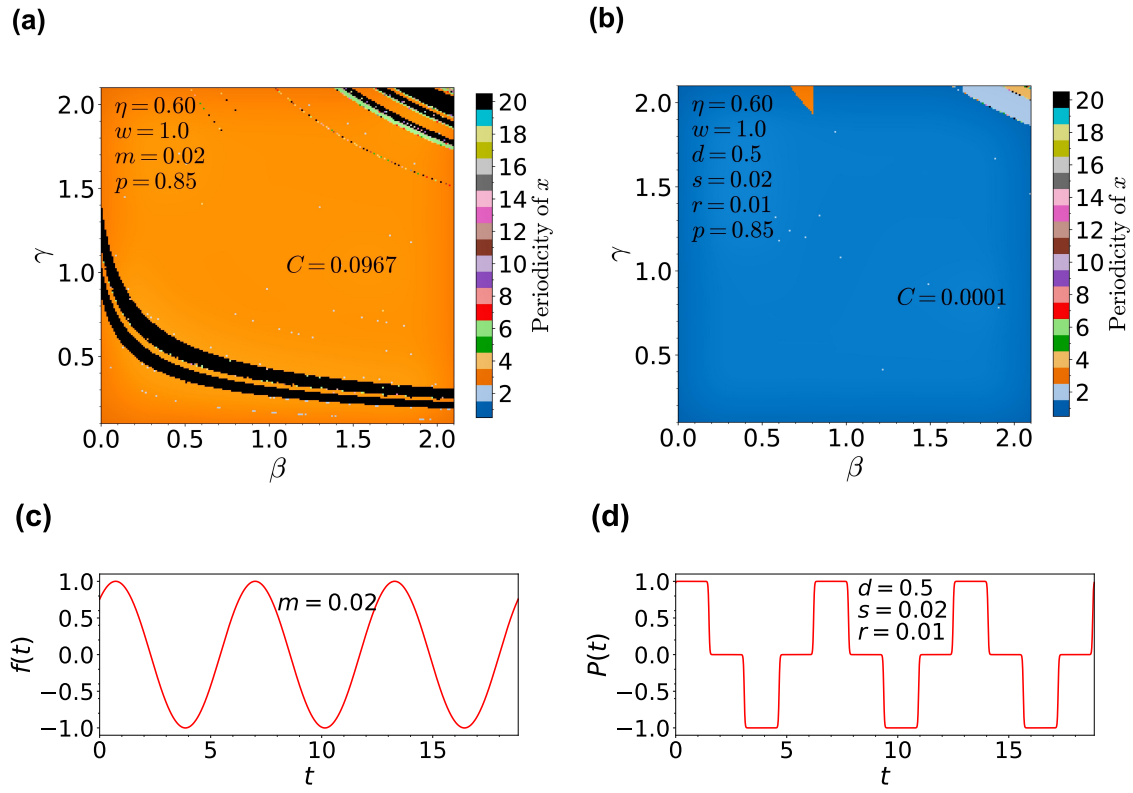


Figure 3.10: (a) and (b) demonstrate the results, where the top panels show 2-dimensional periodograms for both elliptic and periodic pulse functions when control signal $\eta = 0.60$ is applied, and the bottom panels show the corresponding drive signals for the elliptic function (f(t)) using shape parameter $m = 0.02$ (Sinusoidal wave) and the periodic pulse function (P(t)) using smoothness parameter $s = 0.02$ (Smooth square wave). Fixed parameters: $\omega = 1.0$, $p = 0.85$, $d = 0.5$, and $r = 0.01$.

pendent on both the waveform shape and the control amplitude. In the following subsection, the values of C obtained for the elliptic function and the periodic pulse function across the entire (γ, β) parameter plane are compared to more effectively quantify these trends.

3.3.1 Comparison Summary for the Results of Gamma (γ) versus Beta (β) plane

This section presents a comparative analysis of the (γ, β) parameter plane results for both the elliptic function and the periodic pulse function(PPF), with Tables 3.1–3.4 offering a brief comparison of chaos suppression. The degree of chaos in the system is

quantified by the parameter C, which represents the ratio of the chaotic area to the total area of the parameter plane (γ, β). Chaotic regions are defined here as those with periodicities exceeding 20, which correspond to black regions in the periodograms. Therefore, a decrease in C indicates a reduction in the overall amount of chaos, while an increase indicates an expansion of chaotic behaviour within the parameter space.

Table 3.1 provides a baseline comparison corresponding to Fig. 3.5(a,b), when no control signal $\eta = 0$ is applied, and Table 3.2 gives a comparison analysis corresponding

Table 3.1: Chaos Suppression Comparison $\eta = 0$ in the Duffing System

Fig	**Signal Type**	**Shape** (m) **/ Smoothness** s	C	**Chaos Analysis**
3.5(a)	Elliptic	0	0.0839	No Signal
3.5(b)	PPF	0	0.0839	No Signal

Table 3.2: Chaos Suppression Comparison $\eta = 0.03$ in the Duffing System

Fig	**Signal Type**	**Shape** (m) **/ Smoothness** (s)	C	**Chaos Analysis**
3.6(a)	Elliptic	0	0.0935	Increased
3.6(b)	PPF	0	0.0667	Decreased
3.7(a)	Elliptic	0.717	0.0937	Increased
3.7(b)	PPF	0.717	0.0603	Decreased
3.8(a)	Elliptic	0.9999	0.0824	Decreased
3.8(b)	PPF	0.9999	0.0555	Decreased

to Fig. 3.6(a,b), 3.7(a,b) and 3.8(a,b), when a weak control signal $\eta = 0.03$ is applied to the Duffing system. Table 3.3 and Table 3.4 present The results for strong control

Table 3.3: Chaos Suppression Comparison $\eta = 0.30$ in the Duffing System

Fig	**Signal Type**	**Shape** (m) **/ Smoothness** s	C	**Chaos Analysis**
3.9(a)	Elliptic	0.02	0.1001	Increased
3.9(b)	PPF	0.02	0.0279	Decreased

amplitudes, specifically $\eta = 0.30$ and $\eta = 0.60$. In these studies, the Duffing system is driven by a periodic pulse function and an elliptic function, using fixed parameters

$s = 0.02$, $d = 0.5$, $r = 0.01$, $m = 0$, $p = 0.85$, and $\omega = 1.0$. Therefore, Tables 3.2–3.4 enable direct comparisons between the controlled systems and the uncontrolled baseline provided in Table 3.1.

Table 3.4: Chaos Suppression Comparison $\eta = 0.60$ in the Duffing System

Fig	**Signal Type**	**Shape** (m) **/ Smoothness** s	C	**Chaos Analysis**
3.10(a)	Elliptic	0.02	0.0967	Increased
3.10(b)	PPF	0.02	0.0001	Decreased

Table 3.2 summarizes chaos suppression for small control amplitudes $\eta = 0.03$. The periodic pulse function reduces chaos more effectively with smooth waveforms $s = 0.717$ and $s = 0.9999$. On the other hand, the Martinez et al. [25, 26] elliptic function control signal gives little overall reduction in chaos for similar waveform shapes $m = 0.717$ and $m = 0.9999$, implying that chaotic regions are mostly redistributed rather than significantly reduced.

The results summarised in Table 3.3 and Table 3.4 show an even stronger suppression of chaos when the periodic pulse function is applied at larger control amplitudes $\eta = 0.30$ and $\eta = 0.60$. The PPF consistently produces lower values of C than the corresponding elliptic function excitation with smoothness ($s = 0.02$) and symmetry factor ($r = 0.01$). This indicates that, in comparison to the elliptic function approach, the anharmonic periodic pulse function provides greater control performance and a more effective technique for reducing the overall amount of chaos in the Duffing system.

3.4 Results of Delta (δ) versus Gamma (γ) plane

This section presents the results for the (δ, γ) parameter plane, using the same comparative methodology and setup parameters as in the previous (γ, β) analysis. The elliptic function and the periodic pulse function are compared again to check which one works better in suppressing chaos and changing the dynamic behaviour of the Duffing system. By looking at a different parameter plane, we can assess how robust these control strategies are and further investigate how waveform shape influences chaos suppression.

Although this is not the main focus of our study, Fig. 3.11(a,b) shows that shrimps (fractal islands of periodicity) do exist inside the parameter space. We note their appearance here and will not go into detail about studying their structure. In Fig. 3.11(a,b),

the top panels display 2-dimensional periodograms for the elliptic function and periodic pulse function, respectively. Since no control signal is applied ($\eta = 0$), both control schemes correspond to an identical uncontrolled baseline yielding $C = 0.1002$. The bottom panels show drive signals corresponding to each case. Fig. 3.11(c) presents an elliptic function control signal for a shape parameter (m=0), which translates into a sinusoidal waveform. Meanwhile, Fig. 3.11(d) depicts the periodic pulse function at the smoothness parameter (s=0), resulting in a square-wave-like output with a fixed duty cycle and symmetry factor at $d = 0.05$ and $r = 0$, respectively.

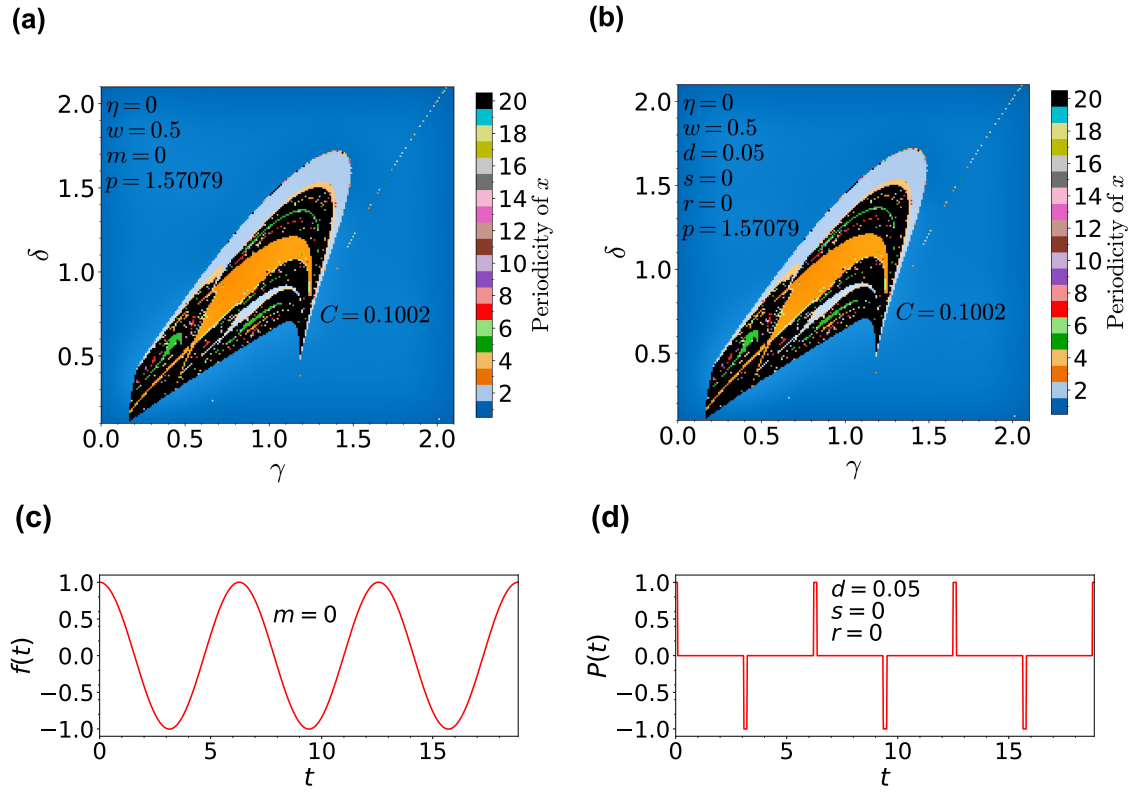


Figure 3.11: (a) and (b) demonstrate the results, where the top panels present 2-dimensional periodogram baseline comparisons between the elliptic function and periodic pulse function (PPF), when no control $\eta = 0$ is applied. These periodograms show shrimps (fractal islands of periodicity) inside the parameter space. Lower panels show corresponding excitation waveforms: (c) elliptic function ($f(t)$) with $m = 0$ sinusoidal waveform, and (d) PPF ($P(t)$) with $s = 0$ square wave-like waveform. Fixed parameters: $\omega = 0.5$, $p = 1.57079$, $d = 0.05$, and $r = 0$.

In Fig. 3.12(a,b), we apply a weak control signal, $\eta = 0.03$, to the top panels of the 2-dimensional periodograms while keeping the shape parameter of the elliptic function and the smoothness parameter of the PPF fixed at $m = 0$ and $s = 0$, respectively. From

Fig. 3.12(a), we note that $C = 0.1034$ is higher than its uncontrolled baseline value of $C = 0.1002$ shown in Fig. 3.11(a); however, in Fig. 3.12(b), $C = 0.0980$ is slightly lower than its baseline value of $C = 0.1002$ from Fig. 3.11(b). The black regions on the periodograms show only small changes but indicate that chaos increases for the elliptic function and decreases for the PPF. The bottom panels show the corresponding drive signal for the elliptic function excitation and the PPF; the waveforms in Fig. 3.12(c,d) are identical to those in Fig. 3.11(c,d), with only the control amplitude modified.

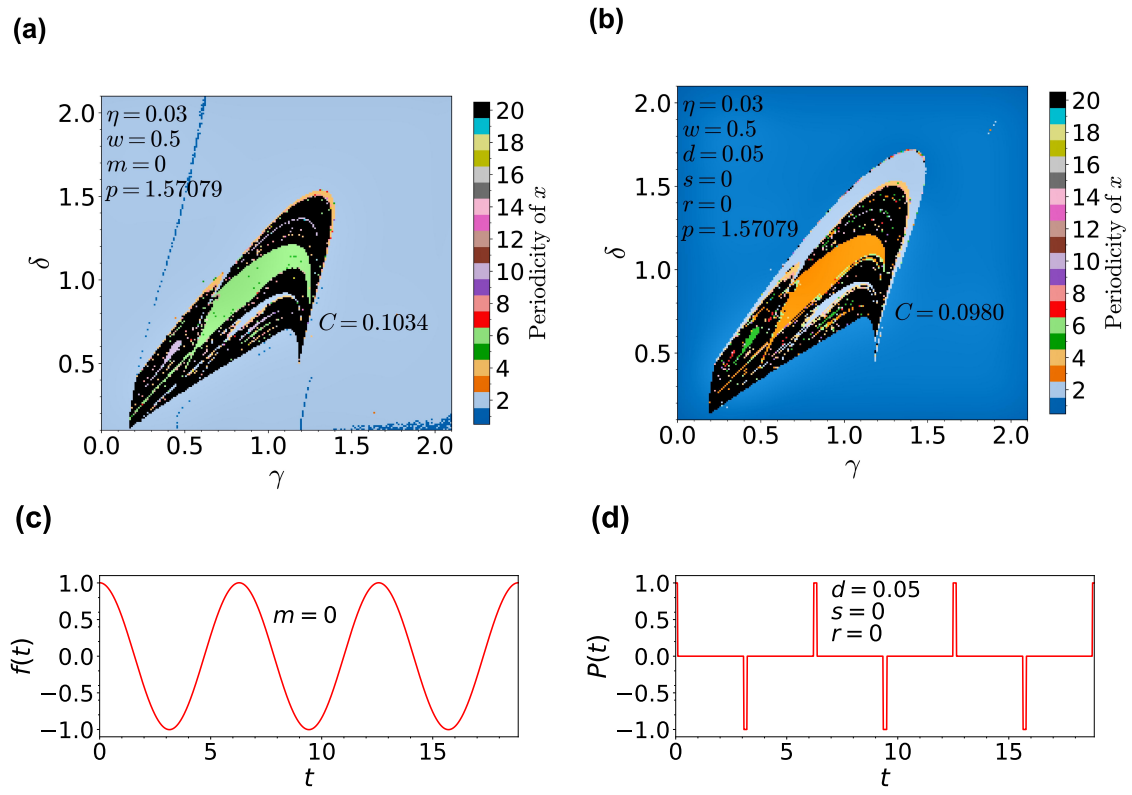


Figure 3.12: (a) and (b) show the results, where the top panels present 2-dimensional periodograms for baseline comparison between the elliptic function and periodic pulse function (PPF), when control amplitude $\eta = 0.03$ is applied. The lower panels demonstrate corresponding excitation waveforms: (c) elliptic function ($f(t)$) with $m = 0$ sinusoidal waveform and (d) PPF ($P(t)$) with $s = 0$ square-wave-like waveform. Fixed parameters: $\omega = 0.5$, $p = 1.57079$, $d = 0.05$, and $r = 0$.

In Fig. 3.13(a,b), we keep the control amplitude fixed at $\eta = 0.03$, but increase the shape parameter of the elliptic function from $m = 0$ to $m = 0.717$ and increase the smoothness parameter of PPF from $s = 0$ to $s = 0.717$. Looking at Fig. 3.13(a), we find that $C = 0.1038$, which is slightly more than what was observed with $C = 0.1034$ in Fig. 3.12(a), and higher than its uncontrolled baseline value $C = 0.1002$ as shown in

Fig. 3.11(a). On the contrary, in Fig. 3.13(b), $C = 0.0819$ is less than both values given by Fig. 3.12(b) and 3.11(b). Hence, increasing the shape parameter further increases chaos for the elliptic function, while increasing the smoothness parameter brings about a substantial reduction of chaos for PPF. The bottom panels show the corresponding drive signals; Fig. 3.13(c) has the excitation by an elliptic function for $m = 0.717$, thus giving a nearly square waveform, while Fig. 3.13(d) shows a PPF waveform when $s = 0.717$, giving a nearly sinusoidal profile.

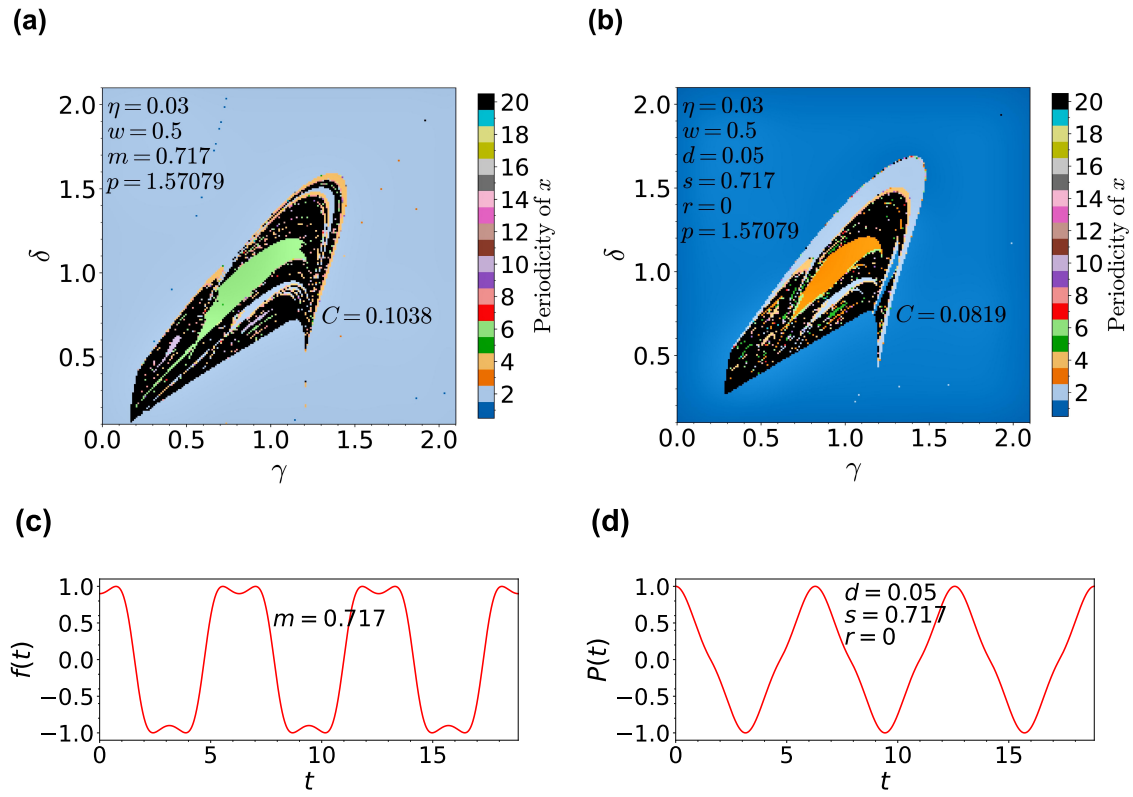


Figure 3.13: (a) and (b) present the results, where the top panels show 2-dimensional periodograms for both elliptic and periodic pulse functions when control signal $\eta = 0.03$ is applied, and the bottom panels demonstrate the corresponding drive signals for the elliptic function (f(t)) using shape parameter $m = 0.717$ (Nearly square wave) and the periodic pulse function (P(t)) using smoothness parameter $s = 0.717$ (Nearly sinusoidal wave). Fixed parameters: $w = 0.5$, $p = 1.57079$, $d = 0.05$, and $r = 0$.

In Fig. 3.14(a,b), the shape parameter and the smoothness parameter are increased further to $m = 0.9999$ and $s = 0.9999$, respectively, while keeping the control amplitude fixed at $\eta = 0.03$. Looking at Fig. 3.14(a), we see that $C = 0.1044$, which is a bit higher than what was obtained in Fig. 3.13(a) $C = 0.1038$, Fig. 3.12(a) $C = 0.1034$, and still higher than the uncontrolled baseline shown in Fig. 3.7(a) $C = 1002$. On

the other hand, Fig. 3.14(b) gives $C = 0.0769$ which is lower than what was obtained in Fig. 3.13(b) $C = 0.819$, Fig. 3.12(b) $C = 0.0980$, and the uncontrolled baseline in Fig. 3.11(b) 0.1002. Even though changes in black regions are fairly small, there is a trend; chaos keeps increasing for the elliptic function, and PPF gives gradually decreasing chaos with increasing smoothness parameter. The bottom panels then show

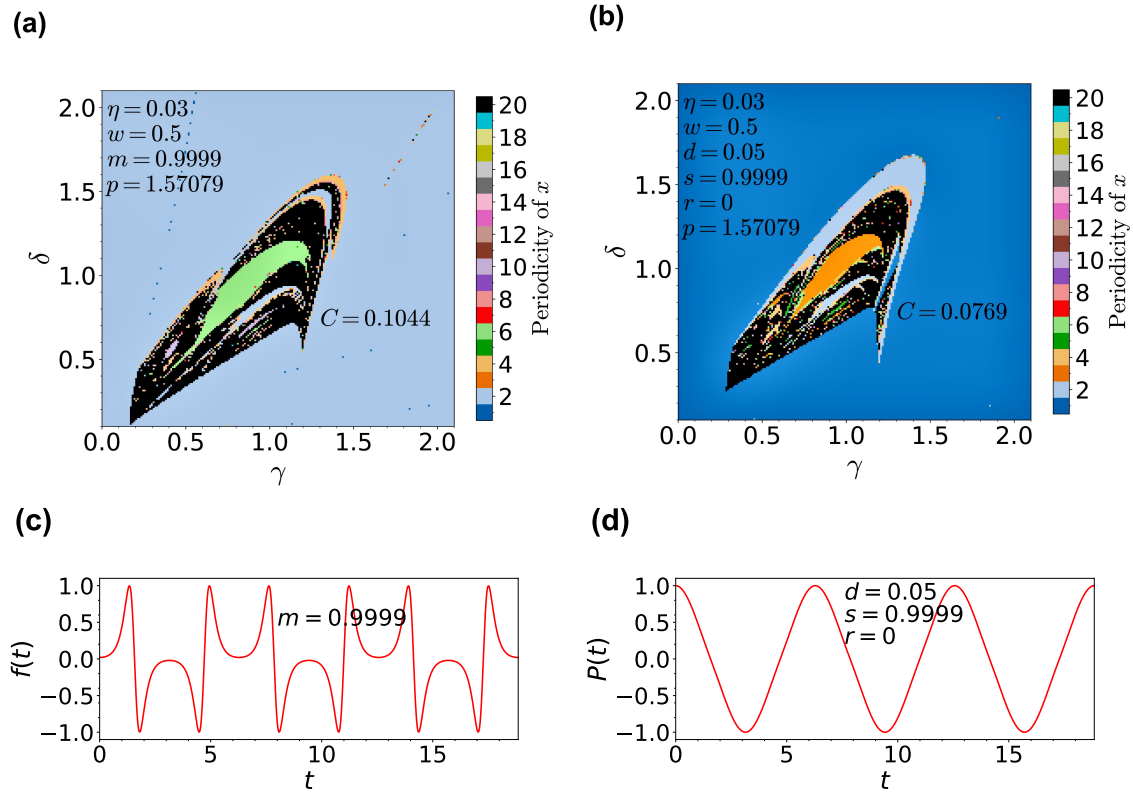


Figure 3.14: (a) and (b) show the results, where the top panels present 2-dimensional periodograms for both elliptic and periodic pulse functions when control signal $\eta = 0.03$ is applied; then the bottom panels show the corresponding drive signals for the elliptic function (f(t)) using shape parameter $m = 0.9999$ (double-humped wave) and the periodic pulse function (P(t)) using smoothness parameter $s = 0.9999$ (smooth sinusoidal wave). Fixed parameters: $\omega = 0.5$, $p = 1.57079$, $d = 0.05$, and $r = 0$.

the corresponding drive signals next to it below; excitation by an elliptic function in Fig. 3.14(c) takes the form of a double-humped waveform when $m = 0.9999$, while PPF in Fig. 3.14(d) gets close to a smooth sinusoidal waveform when $s = 0.9999$, with $d = 0.05$ and $r = 0$ remaining constant throughout.

After examining weak-control cases $\eta = 0.03$, we now use stronger control amplitudes to further test how effective the elliptic function and the periodic pulse function are in suppressing chaos within the (δ, γ) parameter plane. For this analysis, param-

eters are fixed at $m = 0.02$, s= 0.02, $d = 0.5$, $r = 0.01$, $p = 0.85$ and $\omega = 1.0$ while increasing control amplitude to $\eta = 0.30$ and $\eta = 0.60$.

In Fig. 3.15(a,b), an increase in the control amplitude to $\eta = 0.30$ is made, while the shape parameter of the elliptic function and the smoothness parameter of the periodic pulse function are kept fixed at $m = 0.02$ and $s = 0.02$. From Fig. 3.15(a), we note that

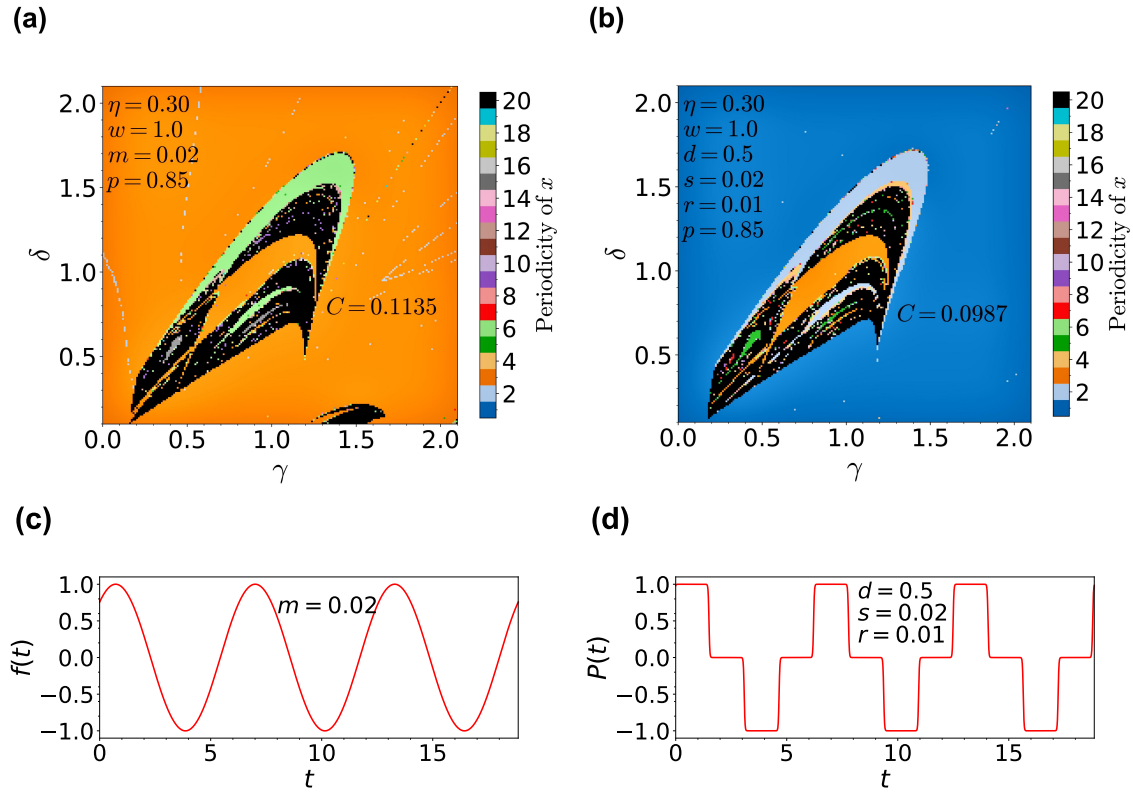


Figure 3.15: (a) and (b) present the 2-dimensional periodograms for the elliptic function and the periodic pulse function (PPF), respectively, with control amplitude fixed at $\eta = 0.30$. Bottom panels show corresponding drive signals: (c) elliptic function excitation $f(t)$ for $m = 0.02$, which is nearly sinusoidal, and (d) periodic pulse function $P(t)$ for $s = 0.02$ resembling a smooth square wave. Fixed parameters are $\omega = 1.0$, $p = 0.85$, $d = 0.5$, and $r = 0.01$.

$C = 0.1135$, which is higher than what was observed with no control in Fig. 3.11(a), where $C = 0.1002$. On the other hand, from Fig. 3.15(b), we see that $C = 0.0987$, which is slightly lower than the baseline value of $C = 0.1002$ shown in Fig. 3.11(b). The black regions on the periodograms indicate small changes, and they also show clearly that chaos increases for the elliptic function but decreases for the periodic pulse function, despite being more prominent at lower parts of the elliptic function parameter plane. The bottom panels show the corresponding drive signals: in Fig. 3.15(c), excitation

by an elliptic function remains approximately sinusoidal for $m = 0.02$; whereas in Fig. 3.15(b), a periodic pulse function keeps its smooth square wave waveform for $s = 0.02$ with fixed duty cycle and symmetry factor at $d = 0.5$ and $r = 0.01$.

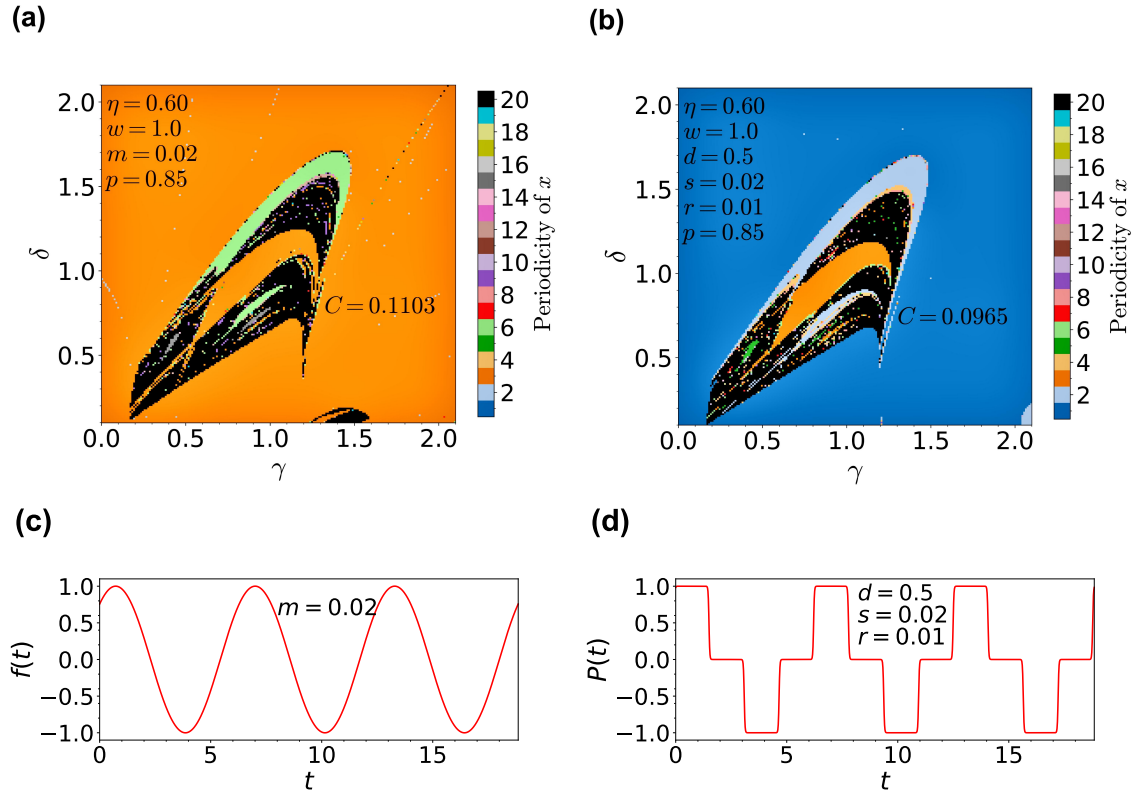


Figure 3.16: (a) and (b) demonstrate the results, where the top panels show 2-dimensional periodograms for both elliptic and periodic pulse functions when control signal $\eta = 0.60$ is applied, and the bottom panels show the corresponding drive signals for the elliptic function (f(t)) using shape parameter $m = 0.02$ (Sinusoidal wave) and the periodic pulse function (P(t)) using smoothness parameter $s = 0.02$ (Slightly smooth square wave). Fixed parameters: $\omega = 1.0$, $p = 0.85$, $d = 0.5$, and $r = 0.01$.

In Fig. 3.16(a,b), we increase control amplitude from $\eta = 0.30$ to $\eta = 0.60$. The shape parameter and smoothness parameter are fixed at $m = 0.02$ and $s = 0.02$. Looking at Fig. 3.16(a), we have $C = 0.1103$; this is slightly less than what was obtained in Fig. 3.15(a), where $C = 0.1135$. However, it is still higher than the uncontrolled baseline value of $C = 0.1002$ seen in Fig. 3.11(a). On the other hand, Fig. 3.16(b) gives us a new result with $C = 0.0965$; this is lower than both results from Fig. 3.15(b) with $C = 0.0987$ and also below the uncontrolled baseline shown in Fig. 3.11(b), $C = 0.1002$. The black regions do not change much, but it appears that this trend continues: further chaos increases for the elliptic function relative to its baseline, while additional reduc-

tions are noted for periodic pulse functions. The bottom panels show the corresponding drive signals: in Fig. 3.16(c), excitation by an elliptic function remains approximately sinusoidal, whereas a periodic pulse function keeps its slightly smooth square wave as was shown in Fig. 3.15(c,d).

Therefore, the results shown by Fig. 3.11–3.16 reveal how much chaos exists in the (δ, γ) parameter plane depends on both waveform shape and control amplitude. The periodograms visually show these changes, but a quantitative comparison is needed for the overall effectiveness assessment of the elliptic function as well as the periodic pulse function. Therefore, the following subsection summarises values of C obtained for each control strategy and compares their ability to reduce chaos relative to the uncontrolled baseline.

3.4.1 Comparison Summary for the Results of Delta (δ) versus Gamma (γ) plane

This section demonstrates a comparative analysis of the (δ, γ) parameter plane results for both the elliptic function and the periodic pulse function(PPF), with Tables 3.5–3.8 highlighting a brief comparison of chaos suppression.

Table 3.5 provides a baseline comparison corresponding to Fig. 3.11(a,b), when no control signal $\eta = 0$ is applied, and Table 3.6 present a comparison analysis corresponding to Fig. 3.12(a,b), 3.13(a,b) and 3.14(a,b), when a weak control signal $\eta = 0.03$ is applied to the Duffing system.

Table 3.5: Chaos Suppression Comparison $\eta = 0$ in the Duffing System

Fig	**Signal Type**	**Shape** (m) / **Smoothness** (s)	C	**Chaos Analysis**
3.11(a)	Elliptic	0	0.1002	No Signal
3.11(b)	PPF	0	0.1002	No Signal

Table 3.7 and Tale 3.8 show the findings for strong control amplitudes $\eta = 0.30$ and $\eta = 0.60$ corresponding to Fig. 3.15(a,b) and 3.16(a,b). Fixed parameters $s = 0.02$, $d = 0.5$, $r = 0.01$, $m = 0$, $p = 0.85$, and $\omega = 1.0$. Therefore, Tables 3.6–3.8 provide direct comparisons between the controlled systems relative to the uncontrolled baseline in Table 3.5.

Table 3.6: Chaos Suppression Comparison $\eta = 0.03$ in the Duffing System

Fig	**Signal Type**	**Shape** (m) / **Smoothness** (s)	C	**Chaos Analysis**
3.12(a)	Elliptic	0	0.1034	Increased
3.12(b)	PPF	0	0.0980	Decreased
3.13(a)	Elliptic	0.717	0.1038	Increased
3.13(b)	PPF	0.717	0.0819	Decreased
3.14(a)	Elliptic	0.9999	0.1044	Increased
3.14(b)	PPF	0.9999	0.0769	Decreased

Table 3.7: Chaos Suppression Comparison $\eta = 0.30$ in the Duffing System

Fig	**Signal Type**	**Shape** (m) / **Smoothness** (s)	C	**Chaos Analysis**
3.15(a)	Elliptic	0.02	0.1135	Increased
3.15(b)	PPF	0.02	0.0987	Decreased

Table 3.8: Chaos Suppression Comparison $\eta = 0.60$ in the Duffing System

Fig	**Signal Type**	**Shape** (m) / **Smoothness** (s)	C	**Chaos Analysis**
3.16(a)	Elliptic	0.02	0.1103	Increased
3.16(b)	PPF	0.02	0.0965	Decreased

The results presented in Tables 3.5–3.8 show that the periodic pulse function consistently performs better in reducing chaotic regions within the Duffing system. On the other hand, excitation of Martinez et al. [25, 26] by the elliptic function generally increases the chaos measure C or shifts chaotic regions in parameter space instead of reducing them. In general, this comparison shows that an anharmonic periodic pulse function is more effective in suppressing chaos than the elliptic function excitation considered in this study. These results further indicate that controlling waveform shape significantly influences phase control strategy effectiveness for nonlinear systems.

Chapter 4

Frequency Locking in the Sine Circle Map

4.1 Introduction

This chapter investigates frequency locking in the sine circle map with harmonic and anharmonic excitations. Frequency locking is a basic characteristic in nonlinear dynamical systems, and it is clearly evident in the sine circle map as the formation of Arnold tongues in parameter space. The sine circle map is entirely harmonic in its traditional formulation. We replace this harmonic excitation with a periodic pulse function (PPF), which signifies anharmonic excitation that involves both fundamental and higher harmonics with non-trivial amplitudes. This carries on from Chapter 3, in which PPF was always found to be better than the control signal based on the harmonic elliptic function at suppressing chaos in the Duffing system. As a result, it is natural to ask if these positive effects would also be applicable to Arnold tongue structures and frequency locking.

Additionally, numerous studies have examined frequency locking in the sine circle map under harmonic excitation, but little has been done on how an anharmonic excitation affects the locking behaviour. As a result, this question is still largely unanswered. Therefore, the purpose of this chapter is to examine how frequency locking and the distributions of locked and chaotic regions in parameter space might be affected by additional anharmonic content introduced by PPF. To answer this question, we first determine the baseline behaviour of the standard sine circle map and the Arnold tongue

structure related to it. Then we introduce the periodic pulse function and explore how its tunable parameter variations, specifically duty cycle (d), smoothness (s), and symmetry factor (r), influence locking dynamics.

Section 4.2 presents the results for the baseline sine circle map. Section 4.3 shows the results for the periodic pulse function circle map. Section 4.4 demonstrates a comparison summary for the results of the standard sine and periodic pulse function circle map, with Table 4.1 comparing the values of C.

4.2 Results of the Standard Sine Circle Map

To iterate the sine circle map (Eq. (2.8)), we represented it by a NumPy array and made use of a standard Python for loop to perform the iterations. The random initial condition, between 0 and 1, was generated by the `uniform` method from the module `random`.

This section presents the findings from the baseline standard sine circle map, which investigates the frequency locking structure associated with Arnold tongues. Similar to Chapter 3, we begin with 1-dimensional bifurcation diagrams and then expand the study to 2 dimensions in a periodogram that covers parameter space globally. The periodicity of the map is indicated by q, with $q = 1$ representing period 1 motion, $q = 2$ representing period 2 motion, etc. The periodicity of q greater than 9 corresponds to chaotic motion. The measure of the extent of chaos within an Arnold tongue structure is C, which is defined as the ratio of the region occupied by chaotic regions ($q > 9$) to the total scanned parameter space.

Fig. 4.1(a) and (c) show 1-dimensional bifurcation diagrams computed from Eq. (2.8) for coupling strengths $K = 0.1$ and $K = 0.6$. The dynamics of weak coupling, $K = 0.1$, are dominated by period 1 motion, with a single branch for $0 \leq \Omega \leq 0.13$ signifying a period 1 locked state. As coupling strength increases to $K = 0.6$, more frequency locking regions appear: around $\Omega \approx 0.35$, three distinct branches of period-3 motion develop, while around $\Omega \approx 0.49$, two branches of period 2 motion are present. These bifurcation diagrams so explicitly demonstrate the periodic states that correspond to the Arnold tongue structure.

Fig. 4.1(b) shows the corresponding 2-dimensional periodogram, where the parameters coupling strength K and winding number Ω are modified simultaneously. The

colour scale corresponds to periodicity q, and white regions represent chaotic motion ($q > 9$). The 0/1 frequency-locked state, which was previously noted as being compat-

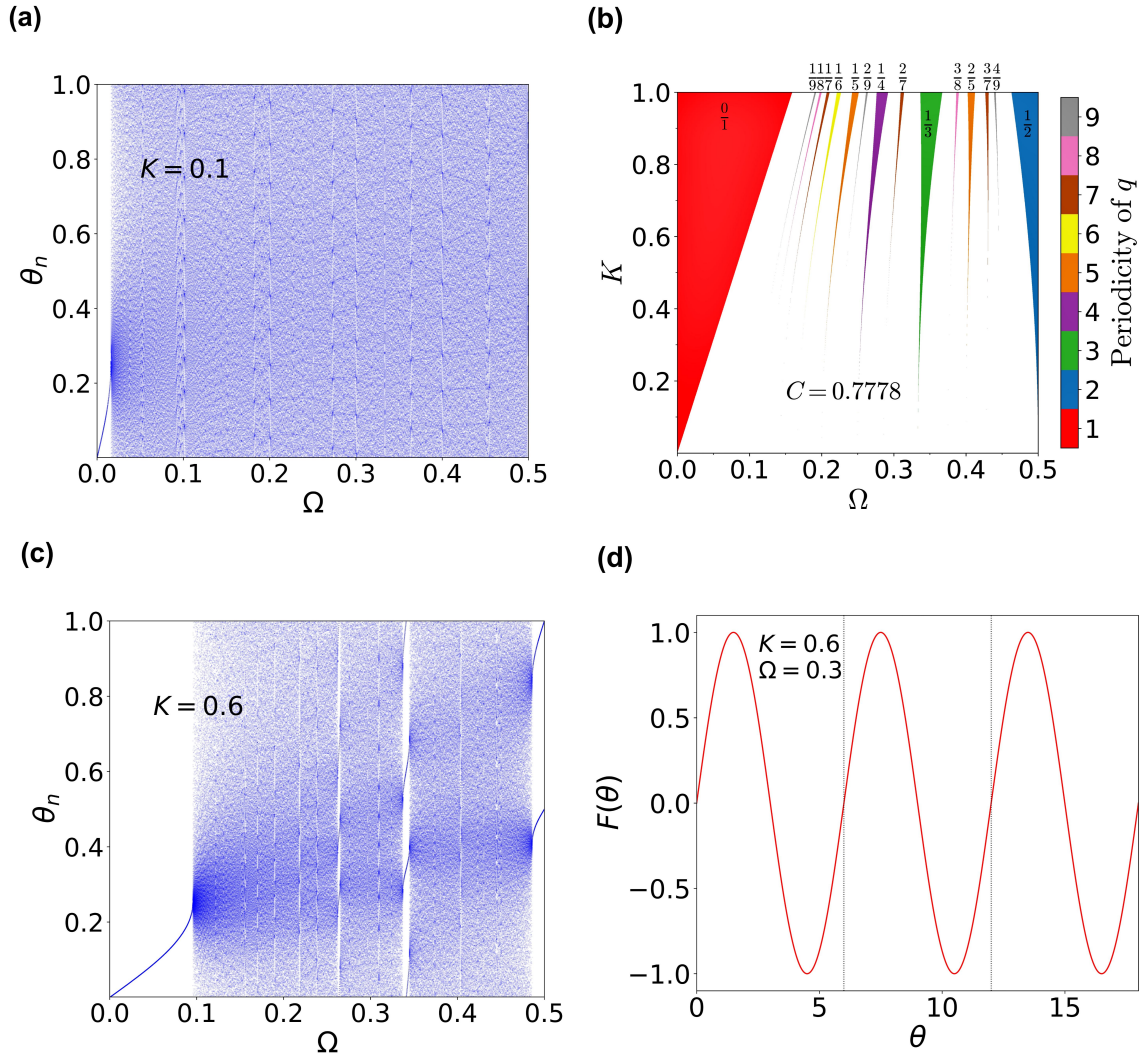


Figure 4.1: (a) and (c) demonstrate the 1-dimensional bifurcation diagrams for the function of winding numbers (Ω) and phase at iteration n (θ_n) corresponding to Eq. (2.8), varying the coupling strength $K = 0.1$ and $K = 0.6$.(b) show the 2-dimensional periodogram of the Arnold tongue structure for the standard sine circle map of $K\Omega$ characteristics, where $C = 0.7778$.(d) present the corresponding sine mapping function, where $F(\theta) = \sin(2\pi\theta)$ (Sinusoidal wave). Fixed parameters: $K \in [0, 1.0]$ and $\Omega \in [0, 0.5]$.

ible with the period 1 branch in Fig. 4.1(a), is linked to the big red tongue stretching from $\Omega = 0$. Similarly, as seen in Fig. 4.1(c), green and blue tongues would be related to 1/3 and 1/2 locking areas, which are connected to period 3 and period-2 branches. The relationship between periodicity and rational winding numbers is consistent with the

Farey-tree organisation of frequency locking discussed by Hilborn et al. [50]. The periodogram shows that chaotic dynamics occupy around 77.78% of the scanned parameter space, indicating a C-value of 0.7778. The remainder are frequency-locked states that exist within the Arnold tongues.

Fig. 4.1(d) illustrates the mapping function related to the standard sine circle map, where $F(\theta) = \sin(2\pi\theta)$, which generates the nonlinear coupling term in Eq. (2.8). The sinusoidal shape of the mapping results in an Arnold tongue structure, shown in Fig. 4.1(b). This is the standard harmonic excitation used in most studies on frequency locking within circle maps. Therefore, the standard sine circle map gives a reference representation of the Arnold tongue structure and the magnitude of chaotic regions in parameter space. The following section will substitute the sinusoidal mapping with a periodic pulse function to investigate how anharmonic excitation affects these frequency locking properties.

4.3 Results of the Periodic Pulse Function Circle Map

This section presents the results of the periodic pulse function (PPF) circle map. The harmonic sine term in Eq. (2.8) is substituted with the periodic pulse function $ppf(\theta)$ given by Eq. (2.29), which depends on three additional tunable parameters, namely duty cycle (d), smoothness (s), and symmetry factor (r). Then Eq. (2.8) becomes

$$\theta_{n+1} = \theta_n + \Omega - \frac{K}{2\pi} ppf(\theta_n, d, s, r) \tag{4.1}$$

We investigate how variations of d, s, and r affect frequency locking and chaos in the Arnold tongue parameter space. The measure C assesses the efficiency of each parameter set for direct comparison with the harmonic sine circle map baseline discussed in Section 4.2. We initially investigate the effect of the duty cycle by varying $d = 0.05$ and $d = 0.4$ while fixing the smoothness $s = 0.2$ and the symmetry factor.

The top panels of Fig. 4.2(a, b) show the corresponding 2-dimensional periodograms of the Arnold tongue structures, while the bottom panels in Fig. 4.2(c, d) present the associated periodic pulse function mappings ($P(\theta)$). In Fig. 4.2(a), the chaotic region is significantly reduced, resulting in $C = 0.5469$, which is lower than the harmonic

sine circle map baseline of $C = 0.7778$ shown in Fig. 4.1(b), yet the Arnold tongues remain large and clearly visible for $d = 0.05$. In Fig. 4.2(b), increasing the duty cycle to $d = 0.4$ increases C to 0.6186. Although this value remains below the baseline, it is substantially higher than the value achieved at $d = 0.05$. This illustrates that lower duty cycles are more effective at reducing chaos and promoting frequency locking regions. In the bottom panels of Fig. 4.2(c, d), the corresponding mapping ($P(\theta)$) for the PPF circle map is shown using the same smoothness as the bottom panel of Fig. 4.2(c) $s = 0.2$, (Sharp square wave-like) and Fig. 4.2(d) $s = 0.2$, (Round square wave-like), but the mapping is different because of the duty cycle effect.

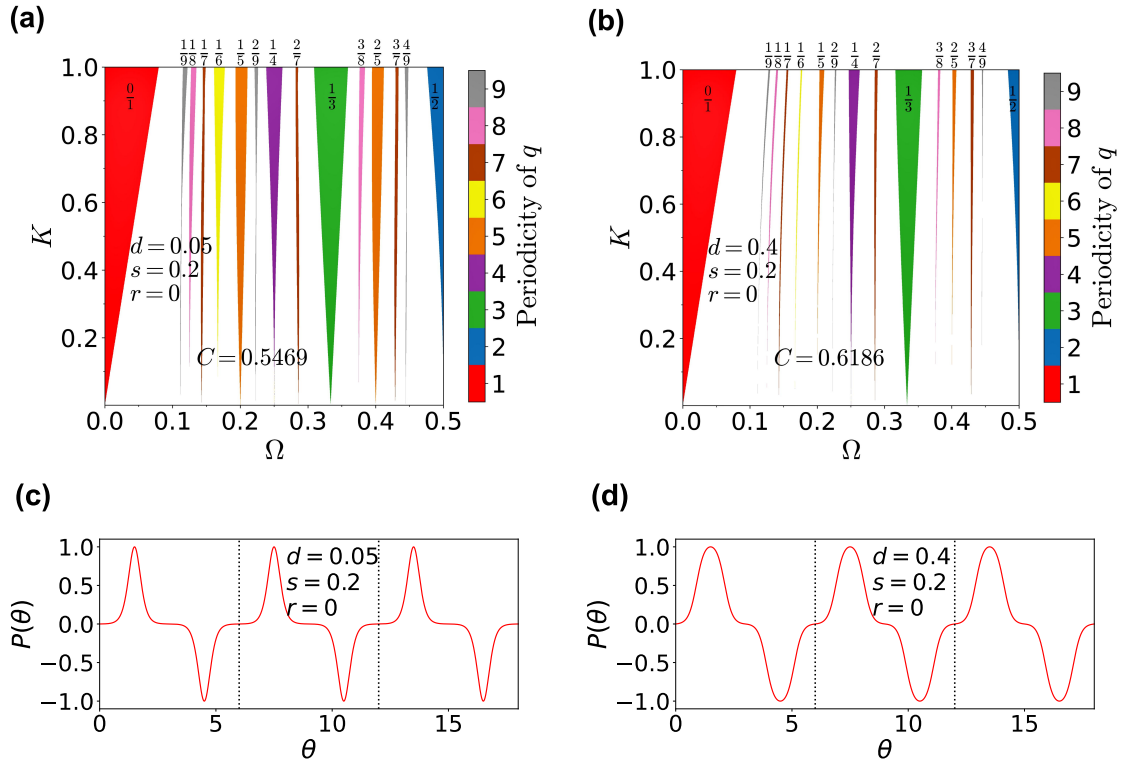


Figure 4.2: (a) and (b) show the results of the 2-dimensional periodogram of the Arnold tongue structures for the PPF circle map when varying the duty cycle: (a) $d = 0.05$ and (b) $d = 0.4$, while fixing the smoothness $s = 0.2$ and symmetry factor $r = 0$. The bottom panels show the corresponding mapping ($P(\theta)$) for the PPF circle map using the same smoothness for (c) $s = 0.2$ (sharp square wave-like) and (b), $s = 0.2$ (Round square wave-like).

We will now look at what happens when low smoothness values are used, with the duty cycle fixed at $d = 0.05$ and symmetry factor $r = 0$. The top panels of Fig. 4.3(a, b) give the Arnold tongue structures for $s = 0.1$ and $s = 0.3$. In Fig. 4.3(a, b), we

vary low smoothness $s = 0.1$ and $s = 0.3$; then, for Fig. 4.3(a), we get $C = 0.5879$, which is a chaotic reduction compared to the baseline in Fig. 4.1(b), where $C = 0.7778$. Increasing the smoothness from $s = 0.1$ to $s = 0.3$ in Fig. 4.3(b) increases C to 0.6022, which is marginally higher than $s = 0.1$ in the top panel of Fig. 4.3(a), but still much lower than the baseline of 0.7778. Chaos is significantly reduced in both cases when compared to the baseline. The Arnold tongues are still visible and slightly reduced in size. The corresponding mappings in Fig. 4.3(c, d) show a gradual transition from a peak square-wave-like profile at $s = 0.1$ to a more rounded square-wave-like profile at $s = 0.3$. This indicates that low smoothness values favour chaos reduction while preserving frequency locking structures.

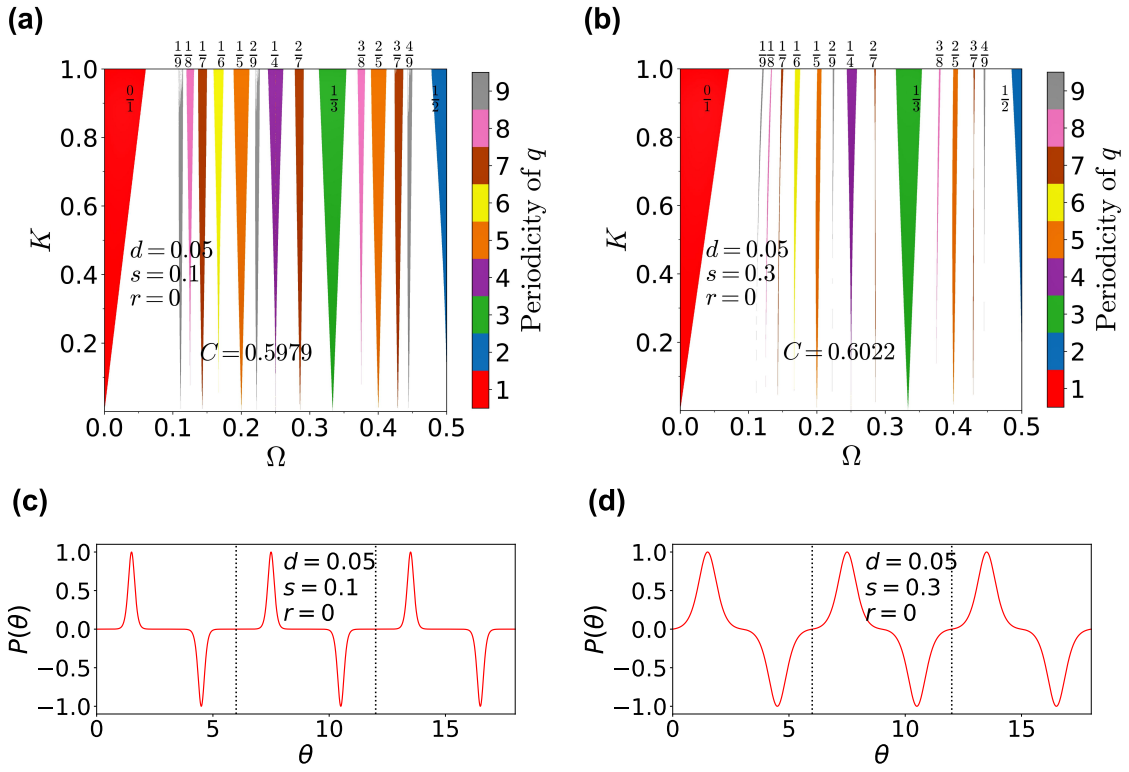


Figure 4.3: (a) and (b) show the results of the 2-dimensional periodogram of the Arnold tongue structures for the PPF circle map when varying low smoothness (a) $s = 0.1$ and (b) $s = 0.3$ while fixing duty cycle $d = 0.05$ and symmetry factor $r = 0$. The bottom panels show the corresponding drive signal ($P(\theta)$) for the PPF circle map using the different smoothness for (c) $s = 0.1$ (peak square-wave-like), and (d) $s = 0.3$ (round square-wave-like).

Next, we consider high smoothness values by increasing s to 0.717 and 0.9999, keeping $d = 0.05$ and $r = 0$ fixed. The corresponding Arnold tongue structures are shown in the top panels of Fig. 4.4(a, b). For $s = 0.717$, Fig.4.4(a) gives $C = 0.7635$,

which is a very small drop from the harmonic baseline value. When smoothness is raised to $s = 0.9999$ in Fig.4.4(b), C increases to 0.7912 and goes beyond the baseline value of $C = 0.7778$, i.e., it increases more than the baseline value of $C = 0.7778$ with an increase in smoothness from $s = 0.717$ to $s = 0.9999$. Further, the Arnold tongues

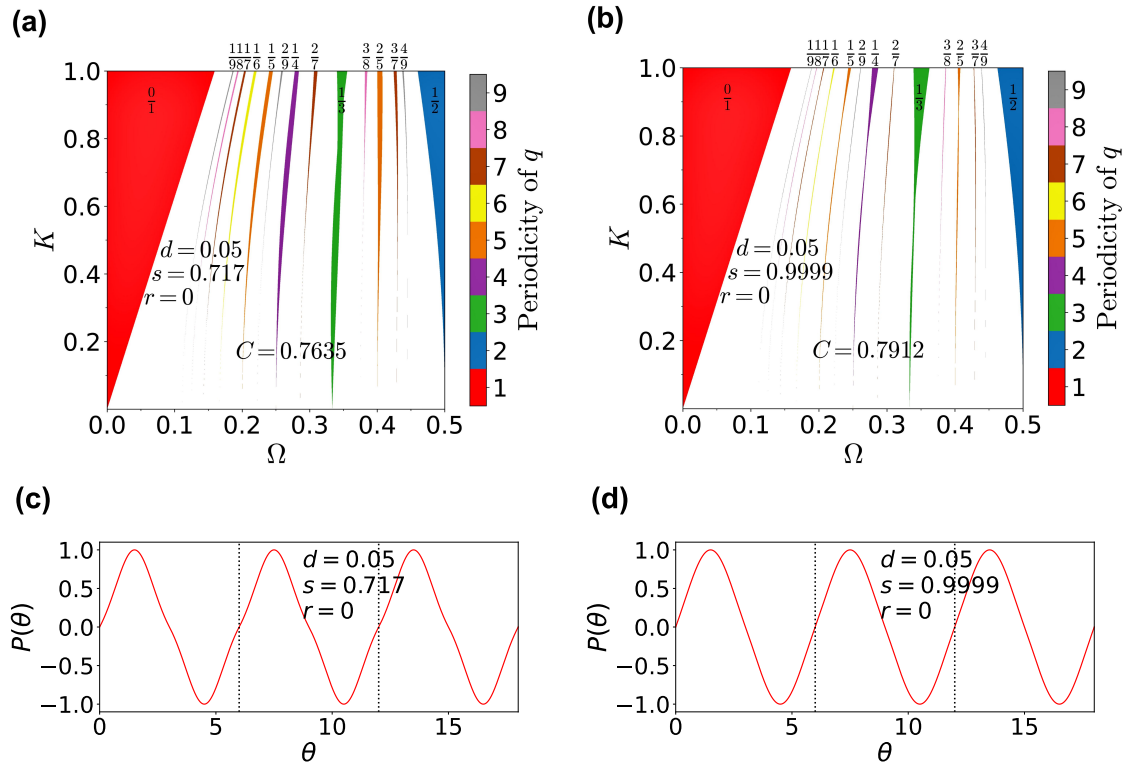


Figure 4.4: (a) and (b) show the results of the 2-dimensional periodogram of the Arnold tongue structures for the PPF circle map when varying high smoothness (a) $s = 0.717$ and (b) $s = 0.9999$ while fixing duty cycle $d = 0.05$ and symmetry factor $r = 0$. The bottom panels show the corresponding drive signal ($P(\theta)$) for the PPF circle map using the different smoothness for (c) $s = 0.717$ (Slightly sinusoidal wave-like), and (d) $s = 0.9999$ (Smooth sinusoidal wave-like).

become thinner and longer as we move towards the centre of parameter space. As we approach $s = 0.9999$, the tongue structure starts looking more similar to that of the standard sine circle map; this behaviour reveals that too much smoothness makes the periodic pulse function lose its anharmonic nature and thus decreases its chaos-suppressing ability and broad frequency locking regions.

This is an interesting trend since it contrasts with what was observed in Chapter 3 for the Duffing system, where larger smoothness values ($s = 0.717$ and $s = 0.9999$) enhanced chaos suppression there but not here. In fact, in our PPF circle map, in-

creasing smoothness pushes the mapping function closer to sinusoidal form so that C takes on larger values, and we get a parameter space structure like that produced by a harmonic sine circle map. This demonstrates how different systems can lead to very opposite behaviours with respect to waveform smoothness. The influence of waveform smoothness depends strongly on the underlying dynamical system

Lastly, we examine the effect of the symmetry factor by fixing $d = 0.05$ and $s = 0.2$. The Arnold tongue structures derived for $r = 0.2$ and $r = 0.4$ are shown in the top panels of Fig. 4.5(a, b). The chaotic region is greatly reduced at $r = 0.2$, resulting

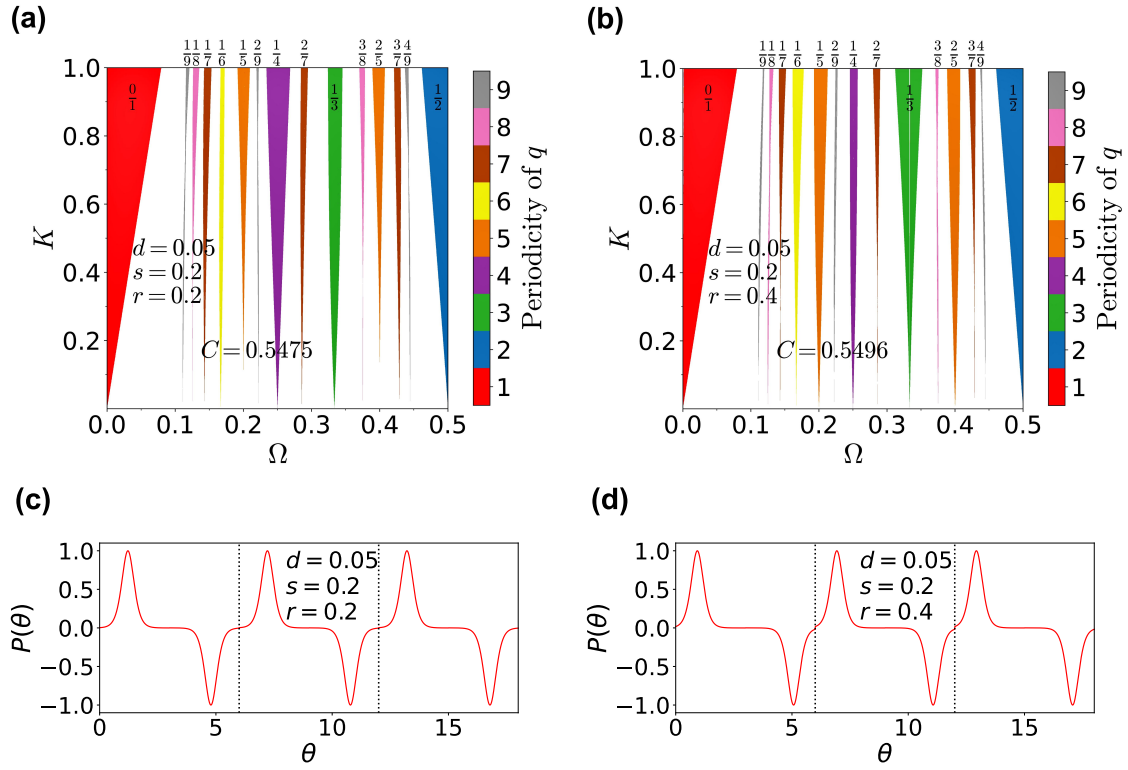


Figure 4.5: (a) and (b) show the results of the 2-dimensional periodogram of the Arnold tongue structures for the PPF circle map when varying the symmetry factor (r): (a) $r = 0.2$ and (b) $r = 0.4$, while fixing the duty cycle $d = 0.05$ and smoothness $s = 0.2$. The bottom panels show the corresponding drive signal ($P(\theta)$) for the PPF circle map using the same smoothness for (c) $s = 0.2$ and (d) $s = 0.2$ (Slightly sharp square wave).

in $C = 0.5475$, which is substantially less than the harmonic baseline $C = 0.7778$. There is just a small increase to $C = 0.5496$ when the symmetry factor is increased to $r = 0.4$. In both cases, broad and distinctly identifiable Arnold tongues indicate that the symmetry factor has only minor effects on general frequency locking structures. In the bottom panels of Fig. 4.5(c, d), the corresponding mapping ($P(\theta)$) for the PPF

circle map uses the same smoothness as the bottom panel of Fig. 4.5(c) $s = 0.2$ and Fig. 4.5(d) $s = 0.2$ which is a slightly sharp square-wave-like shape for both figures.

After looking at how changing the duty cycle, smoothness, and symmetry factor affects Arnold tongue structures in the PPF circle map, we will now compare these results using measure C quantitatively. The next subsection gives an overview of how well each parameter set did compared to the baseline harmonic sine circle map and shows which waveform features work best for reducing chaotic regions, while keeping the frequency locking behaviour intact.

4.4 Comparison Summary for the Results Standard Sine and Periodic Pulse Function Circle Map

This section compares the results for the standard sine map with those from the PPF circle map, with Table 4.1 summarising the frequency-locking results. Section 4.2 discusses the harmonic sine circle map as being dominated by chaotic dynamics with $C = 0.7778$, meaning most of the parameter space lies within chaotic motion ($q > 9$), while frequency locked states ($q < 9$) occur only in relatively narrow Arnold tongues.

Table 4.1: Frequency locking in the Standard Sine and PPF Circle Maps

Fig	**Parameters**	C	**Chaos Analysis**
4.1(b)	Standard sine circle map	0.7778	Baseline
4.2(a)	PPF($d = 0.05,\ s = 0.2,\ r = 0$)	0.5469	Reduction
4.2(b)	PPF($d = 0.4,\ s = 0.2,\ r = 0$)	0.6186	Reduction
4.3(a)	PPF($d = 0.05,\ s = 0.1,\ r = 0$)	0.5979	Reduction
4.3(b)	PPF($d = 0.05,\ s = 0.3,\ r = 0$)	0.6022	Reduction
4.4(a)	PPF($d = 0.05,\ s = 0.717,\ r = 0$)	0.7635	Reduction
4.4(b)	PPF($d = 0.05,\ s = 0.9999,\ r = 0$)	0.7912	Increased
4.5(a)	PPF($d = 0.05,\ s = 0.2,\ r = 0.2$)	0.5475	Reduction
4.5(b)	PPF($d = 0.05,\ s = 0.2,\ r = 0.4$)	0.5496	Reduction

Table 4.1 shows how introducing the anharmonic periodic pulse function changes this balance between chaos and frequency locking, with distinct trends for duty cycle, smoothness, and symmetry factor that help determine best parameter combinations for

chaos reduction. As shown in Table 4.1, the periodic pulse function reduces the chaotic regions in the sine circle map more effectively than the harmonic baseline. The Arnold tongues are broad and well-defined against a significantly reduced chaotic background for low smoothness values and small duty cycle values, when optimal suppression takes place. On the other hand, the mapping becomes more sinusoidal when smoothness is increased to $s = 0.717$ and $s = 0.9999$, leading to larger C values and dynamics that are more similar to those of the standard sine circle map.

Therefore, these findings indicate that, with appropriate parameter selection, the anharmonic periodic pulse function provides an effective method for preserving frequency locking and reducing chaos in the sine circle map. Unlike harmonic sine excitation, which is primarily chaotic, PPF's tunable waveform parameters allow it to substantially affect Arnold tongue topology and increase frequency-locked regions. This highlights the significance of waveform shape in controlling nonlinear dynamical behaviour and frequency-locking-related phenomena.

Chapter 5

Conclusion

This thesis examined how the type of harmonic, anharmonic, and periodic excitation influences chaos control and frequency locking in nonlinear dynamical systems. To systematically examine the role of anharmonicity, a novel periodic pulse function (PPF) was developed, whose duty cycle (d), smoothness (s), and symmetry factor (r) can be independently varied. The periodic pulse function provides a flexible and convenient means of generating periodic excitations with a tunable harmonic spectrum. We used two classical models as prototypes: the sine circle map for discrete dynamics and the Duffing oscillator for continuous dynamics. Both were used as standards for phase control of chaos and frequency locking, respectively.

The key findings summary for Chapters 3 and 4: In Chapter 3 (Phase Control of Chaos in the Duffing System), harmonic (elliptic) driving exhibited minimal suppression and often increased chaos. In contrast, chaos was effectively reduced by anharmonic driving (PPF), even under weak control conditions ($\eta = 0.03$). The periodic pulse function nearly eliminated chaos at large amplitudes ($\eta = 0.30$–0.60), and the sharpness of the pulses (low smoothness) was closely associated with the control's effectiveness, indicating that anharmonicity promoted periodicity and destabilised chaotic attractors. In Chapter 4 (Frequency Locking in the Sine Circle Map), more than 77.78% of the parameter space exhibited chaos due to significant harmonic excitation, with PPF greatly enhancing locking; chaos decreased to approximately 54.69% at ($s = 0.2$), where the duty cycle effectively suppressed it. Large values decreased extensive locking, while small values maintained it. The symmetry factor shifted the Arnold tongues, resulting in moderate reductions in chaos. Smoothness served dual functions: high values ($s = 0.717, 0.9999$)) reinstated chaos above baseline levels, whereas low values

($s = 0.1, 0.2, 0.3$) reduced chaos. Theoretical applications of PPF demonstrated improved locking, as evidenced by the preservation of Arnold tongue structures.

The results reveal a clear insight: harmonic driving cannot reshape non-linear dynamics as anharmonic driving can. The defining features of harmonic excitation are weak locking, narrow tongues, and persistent chaos. On the other hand, anharmonic excitation (PPF) is characterised by significant chaotic suppression, wide locking regions, and control through duty cycle, smoothness, and symmetry. The periodic pulse function thus offers a systematic and flexible basis for frequency locking and chaos control.

Regardless of the wide-ranging insights, the following limitations apply to the scope of this work. The computational cost and execution time of parameter sweeps using high-performance computing (HPC) resources were the two primary numerical constraints. The numerical results took a considerable amount of time to generate and required thorough post-processing to ensure plot accuracy. Therefore, it is possible that some delicate bifurcations and fine Arnold tongue structures were not completely resolved. The present study considered two canonical nonlinear systems, namely the Duffing oscillator and the sine circle map. While these are representative examples and widely used, they do not fully exemplify the intricacies involved in coupled or higher-dimensional nonlinear systems. All analyses were conducted with deterministic models, without any consideration of noise; therefore, in reality, responses may be different when stochastic perturbations, uncertainties, and external disturbances come into play. Another limitation is related to the implementation of the periodic pulse function (PPF). This study idealised the PPF mathematically; however, real-world implementations may have bandwidth limitations and hardware constraints that would affect the resulting waveform. Lastly, this investigation was carried out entirely through numerical simulations, and no experimental setup was used to validate the theoretical and computational findings.

Based on the results, numerous future study directions were identified. Finding the sets of periodic pulse function parameters that will result in optimum chaos suppression requires numerical optimisation and machine learning. Then, while comparing harmonic and anharmonic excitation, systems such as linked oscillators, logistic maps, and Chua's circuit must be considered for generalisations. The performance of the PPF should next be confirmed by testing the resistance of the periodic pulse function control signal to random disturbances and parameter uncertainty using mechanical or electronic testbeds. Lastly, the theoretical expansions for Arnold tongue theory and

bifurcation theory must be appropriately incorporated into anharmonic excitations.

In this thesis, it is demonstrated that the type of excitation (harmonic and anharmonic) affects nonlinear dynamics in the Duffing oscillator and frequency locking. Anharmonic driving through periodic pulse functions (PPF) significantly suppresses chaos, while harmonic driving maintains chaotic behaviour. The anharmonic excitation enhances locking regions and reduces chaos in the sine circle map, in contrast to the limited locking achieved by harmonic excitations. Frequency locking and chaos control with anharmonic excitations through a periodic pulse function result in a versatile and effective tool for controlling nonlinear systems. The study of discrete and continuous prototypes opens new opportunities for real-world applications and theoretical research by establishing anharmonic excitation as a tool for controlling nonlinear dynamics.

Appendix

A.1 Transformation of Simple Pendulum Equation

We start with the original equation of a simple pendulum

$$\frac{d^2\theta}{dt^2} + \frac{g}{l}\sin\theta = 0 \tag{1}$$

where θ is the angle made with respect to the vertical direction, m is the mass of the pendulum, l is its length, and g is the Earth's gravitational acceleration, or equivalently

$$\dot{\theta} = v$$
$$\dot{v} = \frac{g}{l}\sin\theta$$

and a first integral can be obtained by multiplying by $\dot{\theta}$

$$\dot{\theta}\ddot{\theta} + \frac{g}{l}\dot{\theta}\sin\theta = 0 \tag{2}$$

can be written as

$$\frac{d}{\dot{dt}}(\frac{\dot{\theta}^2}{2} - \frac{g}{l}\cos\theta) = 0 \tag{3}$$

where the expression in brackets is multiplied by ml^2, which is the total energy of the pendulum. By assuming $k^2 = \frac{g}{l}$ make substitutions of the transformation: $y = \sin\frac{\theta}{2}$ and linear displacement $\dot{y} = \frac{\dot{\theta}}{2}\cos\frac{\theta}{2} = 0$ thus the differential equation becomes

$$\ddot{y} = \frac{\ddot{\theta}}{2}\cos\frac{\theta}{2} - \frac{\dot{\theta}^2}{4}\sin\frac{\theta}{2} \tag{4}$$

then

$$\ddot{y} = \frac{k^2}{2}\sin\theta\cos\frac{\theta}{2} - \frac{k^2}{2}(\cos\theta - \cos\theta_m)\sin\frac{\theta}{2} \tag{5}$$

and

$$\ddot{y} = -\frac{k^2}{2}\sin(\frac{\theta}{2} + \frac{\theta}{2})\cos\frac{\theta}{2} - \frac{k^2}{2}(\cos(\frac{\theta}{2} + \frac{\theta}{2}) - \cos\theta_m)\sin\frac{\theta}{2} \tag{6}$$

$$\ddot{y} = -k^2 \sin(\frac{\theta}{2}) \cos^2(\frac{\theta}{2}) - \frac{k^2}{2}(\cos^2(\frac{\theta}{2}) - \sin^2(\frac{\theta}{2}) - \cos\theta_m) \sin\frac{\theta}{2} \tag{7}$$

Then

$$\ddot{y} = -k^2 y(1-y^2) - \frac{k^2}{2}(1 - 2y^2 - (1 - 2y_m^2))y \tag{8}$$

simplify Eq. (8)

$$\ddot{y} = -k^2 y(1-y^2) - k^2(y_m^2 - y^2)y = -k^2 y - k^2 y_m^3 + k^2 y^3 + k^2 y^3 \tag{9}$$

therefore,

$$\ddot{y} = -k^2(1 + y_m^2)y + 2k^2 y^3 \tag{10}$$

$$\begin{aligned} a &= -k^2(1 + y_m^2) \\ b &= 2k^2 \\ y_m &= \sin\frac{\theta_m}{2} \end{aligned}$$

where a is the linear coefficient, b is the cubic nonlinear coefficient, and y_m is the maximum transferred displacement. Then Eq. (10) becomes [48]

$$\frac{d^2y}{dx^2} = \ddot{y} = ay + by^3 \tag{11}$$

A.2 Python Code for Periodic Pulse Function

For convenience, we provide a Python implementation of the periodic pulse function given by Eq. (2.29).

```
def ppf(t,d=0.86707122,s=1,r=0):
    '''
    Like sin(t), the periodic pulse function (PPF) has unit amplitude
    and a period of 2*pi. Additional parameters:
        0 <= d <= 1 -- duty cycle
        0 <= s <= 1 -- smoothness factor
        0 <= r <= 1 -- symmetry factor
    Default parameters are set to approximate sin(t) with a
    maximum difference of less than 0.00012. For a square wave,
    set s = 0, i.e. for zero smoothness.
    '''
    with errstate(divide='ignore', over='ignore'):
        eps = 1e-12; d = d + eps
        b = 4*arctan(cos(0.5*t)/sin(0.5*t))/pi; s = 1.75686487/(s+eps)
        p0 = -1/(1+exp(s*(-d-1)))+1/(1+exp(s*(+d-1)))
        a = 1/(1+exp(s*(-d)))-1.0/(1+exp(s*(d))) + p0
        p = 1/(1+exp(s*(abs(b)-d-1+r*(d-1))))-1/(1+exp(s*(abs(b)+d-1+r*(d-1))))
        return sign(b)*(p+p0)/a
```

We also provide the derivative of the periodic pulse function given by Eq. (2.53).

```
def dppf(t,d=0.86707122,s=1.0,r=0.0):
    '''
    The derivative of ppf()
    '''
    with np.errstate(divide='ignore', over='ignore'):
        eps = 1e-12; d = d + eps
        b = 4*arctan(cos(0.5*t)/sin(0.5*t))/pi; s = 1.75686487/(s+eps)
        p0 = -1/(1+exp(s*(-d-1)))+1/(1+exp(s*(+d-1)))
        a = 1/(1+exp(s*(-d)))-1.0/(1+exp(s*(d))) + p0
        p = s*(1/(sqrt(exp(-s*(abs(b)+d-1+r*(d-1)))) \
            +sqrt(exp(s*(abs(b)+d-1+r*(d-1))))))**2 \
            - s*(1/(sqrt(exp(-s*(abs(b)-d-1+r*(d-1)))) \
            +sqrt(exp(s*(abs(b)-d-1+r*(d-1))))))**2
    return -2*p/(a*pi)
```

Figure (1) shows both the above functions as well as the numerically computed derivative for the default parameters.

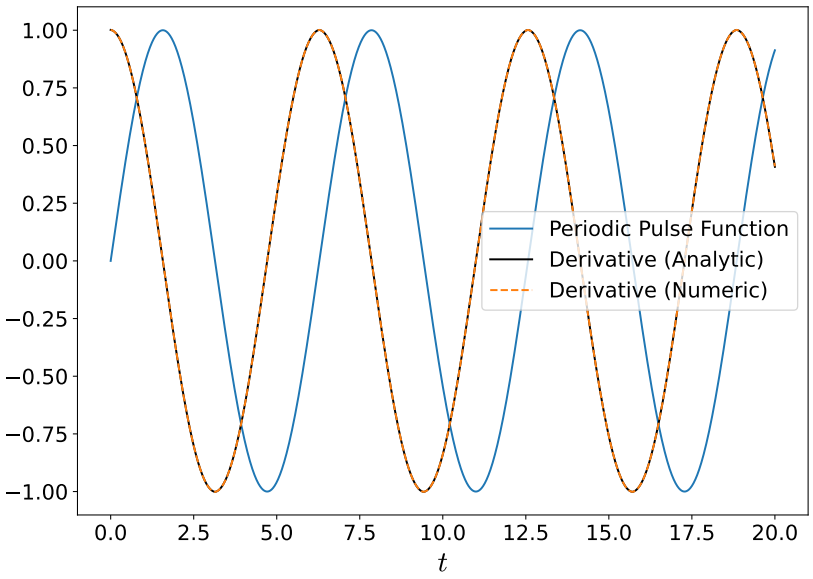


Figure 1: The periodic pulse function and its derivative at the default parameters.

Bibliography

[1] R. L. Kautz, "Noise, chaos, and the Josephson voltage standard," *Reports on Progress in Physics*, vol. 59, no. 8, p. 935, 1996.

[2] V. I. Arnol'd, "Small denominators. I. mappings of the circumference onto itself," in *Eleven Papers on Number Theory, Algebra and Functions of a Complex Variable* (S. I. Adjan *et al.*, eds.), vol. 46 of *American Mathematical Society Translations - Series 2*, pp. 213–284, American Mathematical Society, 1965.

[3] E. Ott, C. Grebogi, and J. A. Yorke, "Controlling chaos," *Physical Review Letters*, vol. 64, no. 11, p. 1196, 1990.

[4] K. Pyragas, "Continuous control of chaos by self-controlling feedback," *Physics Letters A*, vol. 170, no. 6, pp. 421–428, 1992.

[5] D. Auerbach, P. Cvitanović, J.-P. Eckmann, G. Gunaratne, and I. Procaccia, "Exploring chaotic motion through periodic orbits," *Physical Review Letters*, vol. 58, no. 23, p. 2387, 1987.

[6] T. Morita, H. Hata, H. Mori, T. Horita, and K. Tomita, "On partial dimensions and spectra of singularities of strange attractors," *Progress of Theoretical Physics*, vol. 78, no. 3, pp. 511–515, 1987.

[7] C. Grebogi, E. Ott, and J. A. Yorke, "Unstable periodic orbits and the dimensions of multifractal chaotic attractors," *Physical Review A*, vol. 37, no. 5, p. 1711, 1988.

[8] S. Boccaletti, C. Grebogi, Y. Lai, H. Mancini, and D. Maza, "The control of chaos: theory and applications," *Physics Reports*, vol. 329, no. 3, pp. 103–197, 2000.

[9] Z. Qu, G. Hu, G. Yang, and G. Qin, "Phase effect in taming nonautonomous chaos by weak harmonic perturbations," *Physical Review Letters*, vol. 74, no. 10, p. 1736, 1995.

[10] R. Chacón, "Suppression of chaos by selective resonant parametric perturbations," *Physical Review E*, vol. 51, no. 1, p. 761, 1995.

[11] J. Yang, Z. Qu, and G. Hu, "Duffing equation with two periodic forcings: The phase effect," *Physical Review E*, vol. 53, no. 5, p. 4402, 1996.

[12] R. Chacón, "Role of ultrasubharmonic resonances in taming chaos by weak harmonic perturbations," *Europhysics Letters*, vol. 54, no. 2, p. 148, 2001.

[13] H. Cao, X. Chi, and G. Chen, "Suppressing or inducing chaos by weak resonant excitations in an externally-forced Froude pendulum," *International Journal of Bifurcation and Chaos*, vol. 14, no. 03, pp. 1115–1120, 2004.

[14] A. Y. Leung and Z. Liu, "Suppressing chaos for some nonlinear oscillators," *International Journal of Bifurcation and Chaos*, vol. 14, no. 04, pp. 1455–1465, 2004.

[15] R. Meucci, W. Gadomski, M. Ciofini, and F. Arecchi, "Experimental control of chaos by means of weak parametric perturbations," *Physical Review E*, vol. 49, no. 4, p. R2528, 1994.

[16] S. Zambrano, E. Allaria, S. Brugioni, I. Leyva, R. Meucci, M. A. Sanjuán, and F. Arecchi, "Numerical and experimental exploration of phase control of chaos," *Chaos: An Interdisciplinary Journal of Nonlinear Science*, vol. 16, no. 1, p. 1736, 2006.

[17] J. M. Seoane, S. Zambrano, S. Euzzor, R. Meucci, F. T. Arecchi, and M. A. F. Sanjuán, "Avoiding escapes in open dynamical systems using phase control," *Physical Review E*, vol. 78, no. 1, p. 016205, 2008.

[18] S. Zambrano, J. Seoane, I. Marino, M. Sanjuán, S. Euzzor, R. Meucci, and F. Arecchi, "Phase control of excitable systems," *New Journal of Physics*, vol. 10, no. 7, p. 073030, 2008.

[19] R. Chacón, A. M. García-Hoz, J. Miralles, and P. J. Martínez, "Amplitude modulation control of escape from a potential well," *Physics Letters A*, vol. 378, no. 16-17, pp. 1104–1112, 2014.

[20] J. Gonzalez-Henao, E. Pugliese, S. Euzzor, S. Abdalah, R. Meucci, and J. Roversi, "Generation of entanglement in quantum parametric oscillators using phase control," *Scientific Reports*, vol. 5, no. 1, p. 13152, 2015.

[21] J. G. Freire and J. A. Gallas, "Stern–Brocot trees in the periodicity of mixed-mode oscillations," *Physical Chemistry Chemical Physics*, vol. 13, no. 26, pp. 12191–12198, 2011.

[22] E. Pugliese, R. Meucci, S. Euzzor, J. G. Freire, and J. A. Gallas, "Complex dynamics of a dc glow discharge tube: Experimental modeling and stability diagrams," *Scientific Reports*, vol. 5, no. 1, p. 8447, 2015.

[23] L. Junges and J. A. Gallas, "Stability diagrams for continuous wide-range control of two mutually delay-coupled semiconductor lasers," *New Journal of Physics*, vol. 17, no. 5, p. 053038, 2015.

[24] R. Meucci, S. Euzzor, E. Pugliese, S. Zambrano, M. Gallas, and J. Gallas, "Optimal phase-control strategy for damped-driven Duffing oscillators," *Physical Review Letters*, vol. 116, no. 4, p. 044101, 2016.

[25] P. Martínez, S. Euzzor, J. Gallas, R. Meucci, and R. Chacón, "Identification of minimal parameters for optimal suppression of chaos in dissipative driven systems," *Scientific Reports*, vol. 7, no. 1, pp. 1–7, 2017.

[26] P. J. Martínez, S. Euzzor, R. Meucci, and R. Chacón, "Suppression of chaos by incommensurate excitations: Theory and experimental confirmations," *Communications in Nonlinear Science and Numerical Simulation*, vol. 83, no. 1, p. 105137, 2020.

[27] C. Pezeshki and E. Dowell, "An examination of initial condition maps for the sinusoidally excited buckled beam modeled by the Duffing's equation," *Journal of Sound and Vibration*, vol. 117, no. 2, pp. 219–232, 1987.

[28] Y. Chen, "Solution of the Duffing equation by using target function method," *Journal of Sound and Vibration*, vol. 256, no. 3, pp. 573–578, 2002.

[29] Z. Wang, "P-stable linear symmetric multistep methods for periodic initial-value problems," *Computer Physics Communications*, vol. 171, no. 3, pp. 162–174, 2005.

[30] E. Yusufoğlu, "Numerical solution of Duffing equation by the Laplace decomposition algorithm," *Applied Mathematics and Computation*, vol. 177, no. 2, pp. 572–580, 2006.

[31] K. Peleg, "Frequency response of non-linear single degree-of-freedom systems," *International Journal of Mechanical Sciences*, vol. 21, no. 2, pp. 75–84, 1979.

[32] M. Brennan, I. Kovacic, A. Carrella, and T. Waters, "On the jump-up and jump-down frequencies of the Duffing oscillator," *Journal of Sound and Vibration*, vol. 318, no. 4-5, pp. 1250–1261, 2008.

[33] K. Johannessen, "An analytical solution to the equation of motion for the damped nonlinear pendulum," *European Journal of Physics*, vol. 35, no. 3, p. 035014, 2014.

[34] Y. M. Shukrinov, I. Rahmonov, A. Janalizadeh, and M. Kolahchi, "Anomalous Gilbert damping and Duffing features of the superconductor-ferromagnet-superconductor φ 0 Josephson junction," *Physical Review B*, vol. 104, no. 22, p. 224511, 2021.

[35] R. R. Illahi, M. Marzuki, and L. S. Hudha, "Solution of the Duffing equation using exponential time differencing method," *Eigen Mathematics Journal*, vol. 7, no. 1, pp. 16–18, 2024.

[36] M. H. Jensen and S. Krishna, "Inducing phase-locking and chaos in cellular oscillators by modulating the driving stimuli," *FEBS Letters*, vol. 586, no. 11, pp. 1664–1668, 2012.

[37] S. H. Strogatz, *Nonlinear dynamics and chaos: with applications to physics, biology, chemistry, and engineering*. Boca Raton, FL: CRC Press, 2nd ed., 2018.

[38] A. Pikovsky, M. Rosenblum, and J. Kurths, *Synchronization: A universal concept in nonlinear sciences*. Cambridge, UK: Cambridge University Press, 1st ed., 2001.

[39] M. J. Feigenbaum, L. P. Kadanoff, and S. J. Shenker, "Quasiperiodicity in dissipative systems: A renormalization group analysis," *Physica D: Nonlinear Phenomena*, vol. 5, no. 2, pp. 370–386, 1982.

[40] M. H. Jensen, P. Bak, and T. Bohr, "Transition to chaos by interaction of resonances in dissipative systems. I. Circle maps," *Physical Review A*, vol. 30, no. 4, p. 1960, 1984.

[41] S. P. Kuznetsov, *Generalization of the Feigenbaum-Kadanoff-Shenker renormalization and critical phenomena associated with the golden mean quasiperiodicity*. Dordrecht: Kluwer Academic Publishers, 1st ed., 2003.

[42] U. Feudel, C. Grebogi, and E. Ott, "Phase-locking in quasiperiodically forced systems," *Physics Reports*, vol. 290, no. 1-2, pp. 11–25, 1997.

[43] A. Pikovsky and Y. Maistrenko, *Synchronization: Theory and application*. Dordrecht: Kluwer Academic Publishers, 1st ed., 2003.

[44] L. Glass, "Synchronization and rhythmic processes in physiology," *Nature*, vol. 410, no. 6825, pp. 277–284, 2001.

[45] P. D. Donato, E. N. Macau, and C. Grebogi, "Phase locking control in the circle map," *Nonlinear Dynamics*, vol. 47, no. 1, pp. 75–82, 2007.

[46] K. Wiesenfeld, P. Colet, and S. H. Strogatz, "Frequency locking in Josephson arrays: Connection with the Kuramoto model," *Physical Review E*, vol. 57, no. 2, p. 1563, 1998.

[47] K. K. Likharev, *Dynamics of Josephson junctions and circuits*. New York: Gordon and Breach Science Publishers, 1st ed., 1986.

[48] H. T. Davis, *Introduction to nonlinear differential and integral equations*. Washington, D.C.: U.S. Atomic Energy Commission, 1st ed., 1960.

[49] A. H. Salas Salas, J. E. Castillo Hernández, and L. J. Martínez Hernández, "The Duffing oscillator equation and its applications in physics," *Mathematical Problems in Engineering*, vol. 2021, no. 1, p. 9994967, 2021.

[50] R. C. Hilborn, *Chaos and nonlinear dynamics: an introduction for scientists and engineers*. Oxford, New York: Oxford University Press, 2nd ed., 2000.

[51] S. Ostlund, D. Rand, J. Sethna, and E. Siggia, "Universal properties of the transition from quasi-periodicity to chaos in dissipative systems," *Physica D: Nonlinear Phenomena*, vol. 8, no. 3, pp. 303–342, 1983.

[52] X. Wu, Y. Zhang, J. Peng, S. Boscolo, C. Finot, and H. Zeng, "Farey tree and devil's staircase of frequency-locked breathers in ultrafast lasers," *Nature Communications*, vol. 13, no. 1, p. 5784, 2022.

[53] A. Wolf, J. B. Swift, H. L. Swinney, and J. A. Vastano, "Determining Lyapunov exponents from a time series," *Physica D: Nonlinear Phenomena*, vol. 16, no. 3, pp. 285–317, 1985.

[54] G. Bennetin, L. Galgani, A. Giorgilli, and J. Strelcyn, "Lyapunov characteristic exponents for smooth dynamical systems and for hamiltonian systems: A method for computing all of them," *Meccanica*, vol. 15, no. 9, p. 27, 1980.

[55] A. Brandstäter, J. Swift, H. L. Swinney, A. Wolf, J. D. Farmer, E. Jen, and P. Crutchfield, "Low-dimensional chaos in a hydrodynamic system," *Physical Review Letters*, vol. 51, no. 16, p. 1442, 1983.

[56] M. Cencini, F. Cecconi, and A. Vulpiani, *Chaos: From simple models to complex systems*. Singapore: World Scientific, 1st ed., 2010.

[57] A. Pikovsky and A. Politi, *Lyapunov exponents: A tool to explore complex Dynamics*. Cambridge, UK: Cambridge University Press, 1st ed., 2016.

[58] K. B. Oldham, J. C. Myland, and J. Spanier, *An atlas of functions: with equator, the atlas function calculator*. New York, NY: Springer, 2nd ed., 2009.